AnisoMPM: Animating Anisotropic Damage Mechanics

JOSHUAH WOLPER, University of Pennsylvania
YUNUO CHEN, University of Pennsylvania
MINCHEN LI, University of Pennsylvania
YU FANG, University of Pennsylvania
ZIYIN QU, University of Pennsylvania
JIECONG LU, University of Pennsylvania
MEGGIE CHENG, University of Pennsylvania
CHENFANFU JIANG, University of Pennsylvania

Fig. 1. **Anisotropic Feast.** (Left) We tear raw meat to reveal intricate guided fracture along its grain. (Top R.) An orange slice is torn to illustrate the the beautiful radial anisotropy of the fruit. (Bot. R.) A cheese stick is peeled apart to demonstrate the underlying stringy fiber structures intrinsic to mozzarella.

Dynamic fracture surrounds us in our day-to-day lives, but animating this phenomenon is notoriously difficult and only further complicated by anisotropic materials—those with underlying structures that dictate preferred fracture directions. Thus, we present AnisoMPM: a robust and general approach for animating the dynamic fracture of isotropic, transversely isotropic, and orthotropic materials. AnisoMPM has three core components: a technique for anisotropic damage evolution, methods for anisotropic elastic response, and a coupling approach. For anisotropic damage, we adopt a non-local continuum damage mechanics (CDM) geometric approach to crack modeling and augment this with structural tensors to encode material anisotropy. Furthermore, we discretize our damage evolution with explicit and implicit integration, giving a high degree of computational efficiency and flexibility. We also utilize a QR-decomposition based anisotropic constitutive model that is inversion safe, more efficient than SVD models, easy to implement, robust to extreme deformations, and that captures all aforementioned modes of anisotropy. Our elasto-damage coupling is enforced through an additive decomposition of our hyperelasticity into a tensile and compressive component in which damage is used to degrade the tensile contribution to allow for material separation. For extremely stiff fibered materials, we further introduce a novel Galerkin weak form discretization that enables embedded directional inextensibility. We present this as a hard-constrained grid velocity solve that poses an alternative to our anisotropic elasticity that is locking-free and can model very stiff materials.

CCS Concepts: • **Computing methodologies → Physical simulation**.

Additional Key Words and Phrases: Numerical methods, MPM, damage mechanics, fracture, topology change, VFX

ACM Reference Format:
Joshuah Wolper, Yunuo Chen, Minchen Li, Yu Fang, Ziyin Qu, Jiecong Lu, Meggie Cheng, and Chenfanfu Jiang. 2020. AnisoMPM: Animating

Authors' addresses: Joshuah Wolper, University of Pennsylvania; Yunuo Chen, University of Pennsylvania; Minchen Li, University of Pennsylvania; Yu Fang, University of Pennsylvania; Ziyin Qu, University of Pennsylvania; Jiecong Lu, University of Pennsylvania; Meggie Cheng, University of Pennsylvania; Chenfanfu Jiang, University of Pennsylvania.

0730-0301/2020/7-ART37 $15.00
https://doi.org/10.1145/3386569.3392428

Anisotropic Damage Mechanics. *ACM Trans. Graph.* 39, 4, Article 37 (July 2020), 16 pages. https://doi.org/10.1145/3386569.3392428

1 INTRODUCTION

Fracture follows us through our everyday lives, but not all materials break in the same way; this anisotropy arises due to the presence of underlying fibrous structures that govern a material's directional preference for failure. We see examples of this material anisotropy everywhere: strong, stretchy fibers in a steak influence the direction the meat cuts and tears, while a succulent cube of pork belly has decadent layers that peel apart in sheets. Pulling a cheese stick apart is a fun excuse to play with your food but also reveals the underlying stringy fibers that make mozzarella unique, while tearing an orange slice separates and tears the juicy jewels that give it a radial structure.

Fracture is a notoriously difficult phenomenon to model, and naturally, material anisotropy complicates this further. In computer graphics, dynamic anisotropic fracture animation requires methods for large-scale topological deformations, robust schemes for tracking the branching and evolving crack fronts, and a generalizable way to encode and incorporate material anisotropy. There already exist many approaches to animating isotropic fracture in graphics, each with varying degrees of success, but we focus only on those seeking to model the underlying physics of fracture. These physically-based methods have utilized many discretizations: finite element methods (FEMs) paved the way for isotropic brittle and ductile fracture and have seen much exploration since [O'Brien et al. 2002; O'Brien and Hodgins 1999], boundary element methods (BEMs) have recently shown great success for brittle fracture [Da et al. 2016; Hahn and Wojtan 2015, 2016; Zhu et al. 2015], and finally, meshless methods have significantly grown in popularity for material effects like fracture [Pauly et al. 2005; Wolper et al. 2019]. Unfortunately, meshed methods like FEM and BEM require complex and computationally intensive remeshing and node management routines to represent the evolving crack fronts [Molino et al. 2005; Sukumar et al. 2000].

Furthermore, existing approaches to animating anisotropic fracture are limited: Pfaff et al. [2014] achieve anisotropic cracking effects using FEM for thin sheets, but rely on intensive mesh treatments and lack a method for volumetric materials; Hahn and Wojtan [2015] present brittle fractures with anisotropic patterns by spatially modifying material parameters, but BEM lacks ductile fracture and this approach requires the material anisotropy to be explicitly user-defined; most recently, Schrek et al. [2020] present Material Point Method (MPM) based simulation of anisotropic materials composed of macroscopic grains through mapping the anisotropic problem onto an isotropic space for simulation, and while this is an exciting new meshless direction for fracture, it focuses more on anisotropic granular flow and does not seek to model damage. However, from this success we posit that the Material Point Method (MPM) [Sulsky et al. 1995] presents an extremely strong approach for animating anisotropic fracture due to its natural support for arbitrarily large topological deformations, its intrinsic collision handling, and its ever-growing showcase of successfully-animated physical effects.

Though most existing approaches to fracture in graphics focus on fracture mechanics (FM) due to the natural pairing with meshed methods, this requires explicit modeling of crack topology and causes myriad computational challenges. We instead propose to focus on continuum damage mechanics (CDM), characterized by its *smeared crack* approach to modeling fracture. In particular, cracks are represented as continuous fields of evolving damage variables while the material is still considered intact in material space. In world space, the material is weakened based on the damage variables to allow for separation (an approach known as elasticity degradation). Recent works in combining CDM with MPM focus on a non-local CDM technique that utilizes a variational phase-field approach to the *diffuse* crack problem to animate isotropic fracture [Kakouris and Triantafyllou 2017; Wolper et al. 2019]. Although this approach to fracture has been expanded to include anisotropy [Kakouris and Triantafyllou 2018], this requires the incorporation of higher-order damage evolution terms; we deem this excessive for successfully animating anisotropic fracture in graphics. Instead, we propose the exploration of a non-local CDM *geometric* approach to the diffuse crack problem rooted instead in Γ-convergence regularizations of the material discontinuity caused by cracks [Ambrosio and Tortorelli 1990; Miehe et al. 2010b]. This underlying theory led to the derivation of local crack density functions that have seen great success for simulating anisotropic fracture in mechanics [Raina and Miehe 2016; Teichtmeister et al. 2017], and as such, we find it a key tool for anisotropic MPM fracture.

Fig. 2. **Tube Pull.** We stretch a 45 degree fibered tube and show its material space for (a) anisotropic damage and anisotropic elasticity, (b) isotropic damage and isotropic elasticity, (c) anisotropic damage and isotropic elasticity, and (d) no damage and anisotropic elasticity. This illustrates the strength of coupling anisotropic damage with anisotropic elasticity, as only one or the other method leads to weakly guided fracture (c) or numerical fracture (d). Note that (d) does eventually fracture, but it is uncontrollable and numerical.

Although MPM clearly stands as a natural choice of discretization for modeling anisotropic fracture, it has a well-known issue representing material discontinuities. This has spawned many approaches seeking to overcome this problem, namely the compatible particle in cell algorithm (CPIC) for material cutting [Hu et al. 2018a], and

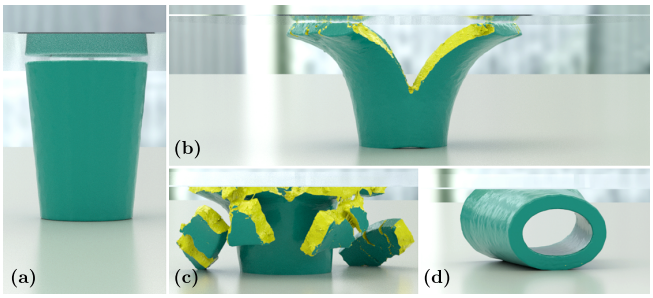

Fig. 3. **Tube Compress.** We compress a vertically fibered tapered tube (a) using (b) anisotropic damage and elasticity, (c) isotropic damage and elasticity, and (d) only anisotropic elasticity. This illustrates successful compressive fracture within AnisoMPM (b,c) and the inability of anisotropic elasticity alone to produce non-numerical fracture (d).

CD-MPM for augmenting MPM with isotropic continuum damage mechanics [Wolper et al. 2019]. Both of these methods lack any semblance of directionality to the producible fractures, thus leaving a wide gap in the literature for the development of a robust and general anisotropic MPM: AnisoMPM. Such an MPM requires three core components to model anisotropic damage mechanics: 1) anisotropic damage state evolution, 2) anisotropic elastic response, and 3) anisotropic mechanical degradation. Fig. 2 and Fig. 3 demonstrate that each of these components struggles to succeed alone.

In mechanics, there exist many approaches to modeling damage in a way that also encodes material anisotropy, including the aforementioned higher order phase field approach. However, we instead focus on what we find to be a simple and highly generalizable way to add anisotropy into our geometric damage model: the structural tensor [Steinmann et al. 1994]. Structural tensors, paired with this geometric approach to fracture, have shown great success for simulating quasistatic anisotropic material failure [Raina and Miehe 2016; Teichtmeister et al. 2017], and as such, we adopt this mechanics theory for AnisoMPM (see §3). Additionally, recall that, in CDM, we represent cracks as a damage gradient in the material space, and this manifests as real discontinuities in world space. However, approaches like CD-MPM struggled greatly with representing these world space cracks due to the particle-based nature of the results. We alleviate this concern by adopting a recently developed MPM meshing algorithm to finely model the cracks produced by AnisoMPM [Wang et al. 2019].

Many works in graphics have sought to model anisotropic elasticity responses in a variety of ways, but we are most inspired by approaches rooted in QR-decomposition due to their robustness and speed [Jiang et al. 2017]. We adapt existing constitutive models to ensure we keep all the desired qualities like inversion safety and robustness, but additionally add terms related to anisotropy that allow us to successfully model isotropy, transverse isotropy, and orthotropy (see §5). This approach also affords us a unique opportunity for elasticity degradation. In particular, the additive decomposition of our hyperelasticity into a tension component and a compression component allows the selective degradation of the tension elasticity, allowing for material separation when damaged. This elasto-damage coupling is key for anisotropic fracture and is enforced through a staggered integration scheme in which damage is evolved and then used to compute grid forces for the grid velocity update. We also present an orthogonal and mutually-exclusive approach to modeling anisotropic elastic response: directional inextensibility. For materials requiring extreme stiffness, it is computationally inefficient to simply rely on the constitutive model to enforce stiffness due to the CFL condition requiring extremely small time steps. Instead, we introduce a locking-free hard-constraint-based inextensibility solver that is incorporated into AnisoMPM as a hard-constrained grid velocity solve, instead of through a constitutive model (see §6).

1.1 Contributions

Our core contribution is the development of AnisoMPM, a robust and general material point method for animating the dynamic fracture of isotropic, transversely isotropic, and orthotropic materials. We evolve damage using a non-local CDM geometric approach paired with structural tensors to encode material anisotropy. Damage is integrated using both explicit and implicit integration for ease of implementation, high efficiency, and computational flexibility. Additionally, since AnisoMPM is an augmentation of traditional MPM it is easy to implement in existing solvers, supports arbitrary constitutive models, and benefits from MPM's natural advantages. AnisoMPM allows a significant level of artistic control through its underlying parameters and clearly has great potential for VFX.

As part of AnisoMPM we use an adapted anisotropic hyperelasticity formulation based on QR-decomposition that not only models all modes of anisotropy, but is also inversion safe, much more efficient than SVD models, simple to implement, and robust under extreme deformations. However, this model lacks robust treatments for materials with extremely stiff fibers and, as such, we develop a novel Galerkin weak form discretization for embedded directional inextensibility that is not only locking-free but also successfully pairs with our damage.

2 RELATED WORK

2.1 Physically Modeling Fracture

For over thirty years, graphics research has grappled with the unique difficulties associated with simulating material fracture [Terzopoulos and Fleischer 1988], leading to a breadth of approaches with varying degrees of success. One of the earliest methods, mass-spring models, represents continuum materials as point masses connected by springs, each with a stress-based yield criterion for fracture [Aoki et al. 2004; Hirota et al. 1998, 2000; Norton et al. 1991]; unfortunately, the resulting fractures suffer from significant artifacts. In [1999], O'Brien and Hodgins successfully modeled brittle fracture using finite element methods (FEMs) and, since then, FEM has proven a promising direction for simulating both brittle and ductile fracture as well as thin shell fracture [Bao et al. 2007; Busaryev et al. 2013; Li et al. 2018; Müller and Gross 2004; O'Brien et al. 2002]. However, these meshed methods require complex mesh treatments to represent the crack topology, including the virtual node algorithm [Molino et al. 2005; Sifakis et al. 2007; Wang et al. 2014], the eXtended finite element method (XFEM) [Koschier et al. 2017; Sukumar et al. 2000], and additional FEM augmentations like Discontinuous Galerkin FEM (DGFEM) [Kaufmann et al. 2008] and level set approaches [Hegemann et al. 2013]. While FEMs focus on

Fig. 4. **Dongpo Pork.** We simulate peeling the top layer of pork belly using three fiber scenarios to demonstrate the unique material effects possible through the defined anisotropy. (Left) We use orthotropic damage and orthotropic elasticity (see §5) to peel away the top layer with damage visualized above. (Middle) We use transverse isotropic fibers to peel away a strip of the top layer. (Right) We show that isotropic damage simply pulls away a small piece of the top layer.

discretizing continuum materials as volume elements, boundary element methods (BEMs) instead focus on modeling the material surfaces and have produced very convincing brittle fracture [Hahn and Wojtan 2015, 2016; James and Pai 1999; Zhu et al. 2015]. Alternatively, some of the most recent approaches obviate meshes entirely, such as element-free Galerkin (EFG) [Belytschko et al. 1995; Lu et al. 1995; Sukumar et al. 1997], clustered shape matching [Jones et al. 2016], and material point method (MPM) [Sulsky et al. 1995]. MPM in particular has proven a successful approach to fracture modeling through augmentations like CRAMP [Nairn 2003], pre-fracture paired with massless particle constraints [Wretborn et al. 2017], focusing on viscoplasticity to facilitate fracture [Pradhana et al. 2017; Stomakhin et al. 2013; Yue et al. 2015], and through material cutting approaches [Hu et al. 2018a]. Most recently, Wolper et al. [2019] combined MPM with continuum damage mechanics (CDM) to model fracture using a non-local phase-field fracture approach.

Though all stem from the same set of seminal fracture theories [Barenblatt 1962; Griffith and Eng 1921; Irwin 1957], most fracture works in graphics focus on fracture mechanics (FM); however, CDM has recently seen more interest in graphics and instead poses a *smeared crack* representation of fracture. Specifically, material discontinuity is tracked in the continuous material (instead of explicitly adding crack geometry) and the material weakens at cracks through elasto-damage coupling [Kachanov 1999]. Within CDM, two core approaches developed in parallel: peridynamics (PD) [He et al. 2018; Levine et al. 2014; Silling 2000; Silling and Askari 2005], and phase-field fracture (PFF) [Aranson et al. 2000; Bourdin et al. 2000; Francfort and Marigo 1998; Miehe et al. 2010b]. PDs seek to avoid the need for derivatives by replacing differential equations with integral ones, and PFFs evolve a field of damage variables over time to model cracks. PFFs in particular have proven successful through their variational approach to *diffuse* crack modeling, and typically perform elasto-damage coupling through elasticity degradation, an approach in which the elastic potential can be additively split into a tension and a compression component with the tension term degraded using the tracked damage variables to allow for material separation [Ambati et al. 2016; Borden et al. 2016; Miehe et al. 2015]. As opposed to the recently-used variational approach to approximating the phase-field surface integral [Bourdin et al. 2008; Wolper et al. 2019], we focus on a geometric approach rooted in Γ-convergence regularizations of free discontinuity problems [Ambrosio and Tortorelli 1990; Miehe et al. 2010b]. These methods are characterized by the introduction of *crack surface density functions* that measure spatially regularized crack surfaces and have been used at length for phase-field fracture in mechanics [Miehe et al. 2015; Raina and Miehe 2016; Teichtmeister et al. 2017].

2.2 Anisotropic Damage

Within CDM, there exist many approaches to modeling anisotropic damage, each having application-specific considerations. While virtually every method focuses on damage through elasto-damage coupling, each has a unique means of tracking and evolving damage. Multi-damage variable approaches track more than a single variable to represent different types of material damage: one approach models damage variables for the material matrix and fibers separately [Calvo et al. 2007], while a longitudinal/transverse damage model tracks two orthogonal components of damage to model orthotropy [Bleyer and Alessi 2018]. Conversely, some models forgo damage variables entirely in favor of an evolving second order damage tensor to encode anisotropic damage [Fassin et al. 2018; Ito et al. 2010; Nairn et al. 2017]. Other approaches are more biologically inspired and focus on damaged fiber density to compute damage [Natali et al. 2005], while others focus on the multiplicative decomposition of the deformation gradient into a plastic part, an elastic part, and a damage part that evolves over time [Shanthraj et al. 2017]. Recently, global-local approaches were developed to locally evolve a phase-field and then solve a linear elastic problem globally to evolve damage, but these require adaptive domain decomposition routines that present lengthy overhead [Gerasimov et al. 2018; Noii et al. 2019]. Finally, it has been shown that anisotropic plasticity can be a successful approach to modeling anisotropic damage, particularly through the anisotropic Tsai-Hill yield surface [Korenczuk et al. 2017], and modeling the granular flow of anisotropic grains using anisotropic Drucker-Prager [Daviet and Bertails-Descoubes 2016].

Pairing CDM with MPM has seen exploration in mechanics, particularly in approaches such as damage gradient partitioning (DGP) to define crack paths [Homel and Herbold 2017; Moutsanidis et al. 2019]; however, this requires currently undeveloped treatments to align the failure planes in the material and the damage gradient. Conversely, anisotropic damage within MPM has been successfully

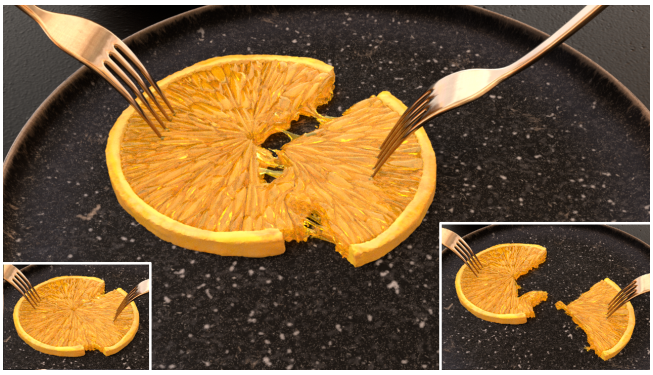

Fig. 5. **Orange Tear.** We pull apart a multi-material orange slice simulated with radial fibers for anisotropic damage. This demonstrates a material where anisotropic damage alone produces photo-real results.

modeled in the quasistatic setting for brittle fracture by employing a fourth-order phase-field evolution equation [Borden et al. 2014; Kakouris and Triantafyllou 2018]. Unfortunately, this not only poses extremely expensive computational overhead for updating the phase-field, but also focuses only on modeling the anisotropy of the fracture energy, rather than presenting a mechanically rigorous and unified model of material anisotropy [Bleyer and Alessi 2018]. Alternatively, methods derived from the aforementioned crack density functions typically evolve a field of damage variables by adopting a second-order structural tensor that can be easily incorporated into a damage driving function [Dhas et al. 2018; Raina and Miehe 2016; Steinmann et al. 1994; Teichtmeister et al. 2017]. These structural tensors are easy to implement, robust, and highly generalizable in that they can capture isotropy, transverse isotropy, orthotropy, and even cubic symmetry [Teichtmeister et al. 2017]. For this reason, we choose to explore anisotropic damage by pairing structural tensors with a second order crack density function (higher orders exist, but are qualitatively unnecessary) [Raina and Miehe 2016].

2.3 Anisotropic Elasticity

Elasticity is a key component in modeling material responses. Isotropic constitutive models have seen extensive study in graphics [Bouaziz et al. 2014; Smith et al. 2018; Stomakhin et al. 2012]. However, since many materials are inherently direction-dependent, anisotropy must be incorporated for the realistic simulation of these materials, including cloth [Jiang et al. 2017], plants [Wang et al. 2017], and biological tissues [Chagnon et al. 2015; Raina and Miehe 2016; Teran et al. 2003]. In recent years, many anisotropic elasticity models have been designed in graphics to model different cases of anisotropic behaviors. This includes transverse isotropic elasticity [Kim et al. 2019], in which a single fiber direction is stiffened per quadrature, as well as orthotropic elasticity [Li and Barbič 2015] where material properties can differ along all three orthogonal axes. A variety of approaches have been proposed by researchers in modeling anisotropy. For example, Garcia-Gonzalez et al. [2018] use structural tensors to derive anisotropic elasticity, while Chen et al. [2018] use shape function modifications to model elasticity. Alternatively, Jiang et al. [2017] propose a model based on the QR-decomposition of strain that is specifically designed for co-dimensional objects with explicit time integration. We generalize this QR-based design to arbitrary volumetric models which can be reduced to stable Neo-Hookean [Smith et al. 2018], and potentially any arbitrary anisotropic elasticity.

2.4 Inextensibility

In mechanics, inextensiblity theory has been developed to serve as a hard constraint approach to modeling anisotropic materials that have high stiffness in specific directions [O'Bradaigh and Pipes 1991]. As noted by [Babuška and Suri 1992], numerical methods like FEM cannot solve extreme constraints by fulfilling them approximately (such as through using a penalty method); this can lead to the classic *locking* phenomenon. Thus, for these materials, inextensibility theory with hard constraints is preferred. In recent years, new approaches have arisen to overcome this difficulty. Solving the locking problem has seen much exploration: Wriggers et al. [2016] developed a locking-free finite element theory for large strain anisotropic behavior using the Lagrange multiplier method, and recently, Chen et al. [2019] introduced a set of simple meshless isometry constraints to avoid the locking problem in simulating inextensible thin-plate materials. Inextensibility has also attracted attention in graphics, since many materials have underlying fiber structures. Some theories have proven successful for simulating inextensible materials like cloth [Goldenthal et al. 2007; Harmon et al. 2009] and hair [Bertails et al. 2006; Müller et al. 2012]. Additionally, Tournier et al. [2015] explored inextensibility with stable constraint dynamics using geometric stiffness.

2.5 Material Point Method

Since its inception [Sulsky et al. 1994, 1995], MPM has shown to be an extremely robust and widely-applicable approach for simulating a breadth of both solid and fluid physical phenomena. Though originally formulated for computational fluid dynamics [Brackbill and Ruppel 1986; Zhu and Bridson 2005], MPM has been generalized to solid mechanics in a way that has cemented it as one of the most widely-used choices of discretization for physically-based animation. Successful effects include sand [Daviet and Bertails-Descoubes 2016; Klár et al. 2016; Yue et al. 2018], snow [Stomakhin et al. 2013], foam [Ram et al. 2015; Yue et al. 2015], cloth [Fei et al. 2018; Guo et al. 2018; Jiang et al. 2017], solid-fluid sediment mixtures [Gao et al. 2018a; Pradhana et al. 2017], phase change [Stomakhin et al. 2014], viscoelastic materials [Fang et al. 2019], and, most recently, isotropic fracture [Wolper et al. 2019].

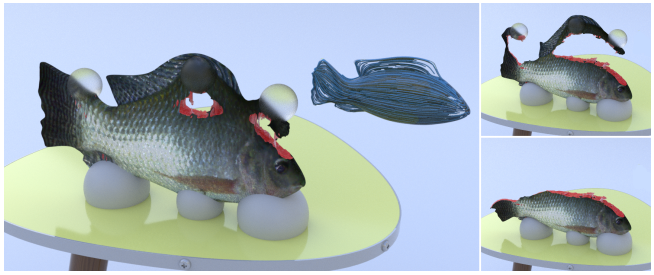

Fig. 6. **Fish Skinning.** We simulate skinning a fish in AnisoMPM using flow-generated fibers for anisotropic damage and anisotropic elasticity.

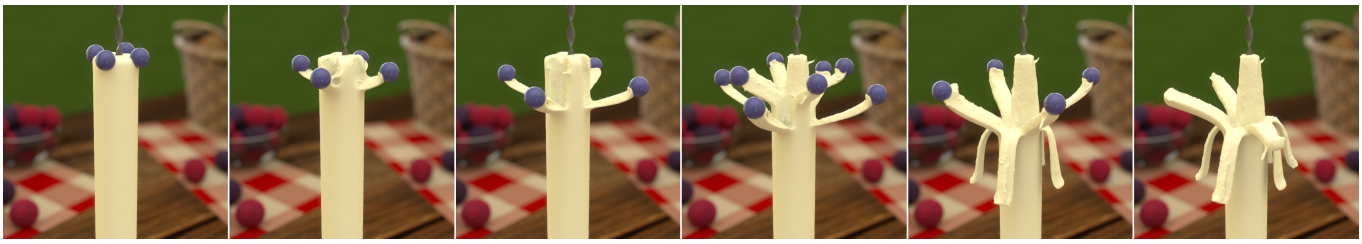

Fig. 7. **String Cheese.** We use transverse isotropic damage and elasticity to peel a mozzarella cheese stick eight ways to reveal the underlying stretchy fibers.

3 ANISOTROPIC DAMAGE

3.1 Geometric Crack Modeling

We begin by defining an elastic body with material space Ω^0 and deformed space Ω^t using the deformation map $\boldsymbol{x} = \phi(\boldsymbol{X}, t)$ with $\boldsymbol{x}$ and $\boldsymbol{X}$ being world and material coordinates respectively. For later use we also denote the material deformation gradient as $\boldsymbol{F} = \frac{\partial \phi}{\partial \boldsymbol{X}}$. We additionally define the crack phase-field as a set of damage variables $d \in [0, 1]$ such that $d = 0$ for unbroken material, and $d = 1$ for fully broken material. Further, to describe the material cracks we are inspired by the geometric approach to diffuse crack modeling outlined in [Miehe et al. 2010b] and adopt the notion of a spatially regularized crack surface functional, $\Gamma_{l_0}(d)$, such that:

$$\Gamma_{l_0}(d) = \int_{\Omega^0} \gamma_{l_0}(d, \nabla d) \mathrm{dV}, \tag{1}$$

where l_0 is a length scale parameter used to regularize the diffuse crack, and γ_{l_0} is a crack surface density function that defines the crack density per unit volume and has the form:

$$\gamma_{l_0}(d, \nabla d) = \frac{d^2}{2l_0} + \frac{l_0}{2}|\nabla d|^2 \mathrm{dV}. \tag{2}$$

This crack surface density function is the key to modeling crack propagation; specifically, the minimization principle of diffuse crack topology gives an expression for the regularized crack phase field as follows:

$$d(\boldsymbol{X}, t) = \arg\{\inf_{d \in W_\Gamma} \Gamma_{l_0}(d)\}, \tag{3}$$

where $W_\Gamma = \{d \mid d(\boldsymbol{X}, t) = 1 \text{ at } \boldsymbol{X} \in \Gamma(t)\}$ is a constraining Dirichlet condition on the damage that ensures damage is maximized on the crack surface. Although higher order crack surface density functions exist, Eqn. 2 has shown success for anisotropic fracture [Raina and Miehe 2016], and was developed by Miehe et al. [2010b] to model the exponential function $\exp(-|x|/l_0)$ as the solution to Eqn. 3 (see Fig. 8 for intuition on why this expression is useful for describing a diffuse crack). This density function assumes that the exact crack, Γ, exists at $x = 0$, and notice in Fig. 8 that changing the regularization parameter changes the spread of the diffuse crack representation. In MPM, this regularization parameter must not exceed the grid resolution, and as such we set it exclusively to be $l_0 = \Delta x/2$ to ensure it never causes the diffuse crack to spread further than one cell; in the interest of keeping the parameter space tractable, we did not explore this parameter further.

The evolution of the damage field can be formulated as a function of the damage, its gradient, and a local crack driving force field, $\tilde{\mathcal{H}}$, that is dependent on the entire history of the material. Specifically, we use the resulting local damage evolution equation that arises from the minimization principle of diffuse crack topology [Miehe et al. 2015]:

$$\eta \dot{d} = (1 - d)\tilde{\mathcal{H}} - D_c. \tag{4}$$

Here, η is a mobility constant that physically controls the viscosity of the crack evolution. The first term on the right is the local crack driving force and the second term is a geometric crack resistance, D_c; thus, the evolution of the damage field is a balance between a driving force, $(1-d)\tilde{\mathcal{H}}$, and a geometric resistance, D_c, with damage only occurring when the former exceeds the latter. By taking the variational derivative of Eqn. 2 we further attain a function for the geometric crack resistance, $D_c = d - l_0^2 \Delta d$, where Δd is the Laplacian of d (we use $\Delta = \nabla^2$).

As cracks evolve and propagate in the material we must also ensure that the cracks are irreversible (cracks never heal) or more specifically, $\dot{\Gamma}_{l_0}(d) \geq 0$. This is achieved through three constraints: bounding the phase field $d \in [0, 1]$, ensuring local crack growth $\dot{d} \geq 0$, and enforcing a positive driving force $\tilde{\mathcal{H}} \geq 0$. By considering a rate independent crack evolution ($\eta = 0$) with homogeneous damage ($\nabla d = 0$) we can manipulate Eqn. 4 and get the following relationships: for $d = 0$ (healthy state) $\tilde{\mathcal{H}} = 0$, for $d = 1$ (maximum damage) $\tilde{\mathcal{H}} = \infty$, and $\dot{\tilde{\mathcal{H}}} \geq 0$. Thus, $\tilde{\mathcal{H}}$ must be a positive, monotonically growing function. We satisfy the third condition through defining $\tilde{\mathcal{H}}$ as the history dependent maximum of a generalized crack driving state function, $\tilde{D}$ like so:

$$\mathcal{H}(\boldsymbol{X}, t) = \max_{s \in [0, t]} \tilde{D}(state(\boldsymbol{X}, s)) \geq 0. \tag{5}$$

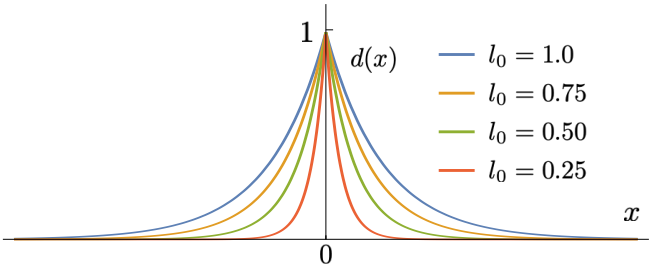

Fig. 8. **Effect of Regularization Parameter on Damage Field.** Here we plot four diffuse cracks at $x = 0$ to illustrate that the diffuse crack representation widens as l_0 increases. These damage plots are of the form $\exp(-|x|/l_0)$ and result from the minimization principle of diffuse crack topology (solving Eqn. 3 using Eqn. 1).

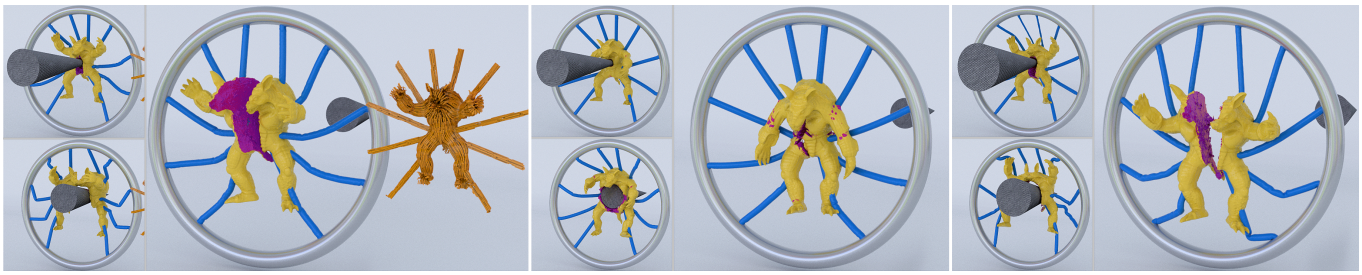

Fig. 9. **Armadillo Lance.** We pierce a soft toy armadillo with a lance using flow-generated fibers to direct (a) anisotropic damage and anisotropic elasticity for the ropes, (b) isotropic damage and anisotropic elasticity ropes, and (c) anisotropic damage and inextensible ropes. This illustrates the clean, bisecting fracture achievable only with anisotropic damage as well as the successful pairing of our damage model with inextensibility.

Here, s is some time in the interval $[0, t]$ with t being the current time. The state function is used to indicate the modularity of this expression: $\tilde{\mathcal{H}}$ is simply defined to be the maximum value of $\tilde{D}$ over all material states during the simulation history. In this way, we can design any crack driving force $\tilde{D}$ as long as it satisfies the aforementioned constraints. The third constraint is already fulfilled by taking the maximum over the material history, but the first and second constraints also require that $\tilde{D} = 0$ for an unbroken state, and $\tilde{D} = \infty$ for a broken state. Ultimately this leads to our final local damage evolution equation:

$$\dot{d} = \frac{1}{\eta} \left\langle (1-d)\tilde{D} - (d - l_0^2 \Delta d) \right\rangle, \tag{6}$$

with $\langle x \rangle := (x + |x|)/2$ as the Macauley bracket, further enforcing the irreversibility of the crack evolution. Now all that is missing is a function for our crack driving force $\tilde{D}$.

3.2 Anisotropic Crack Driving Force

We add anisotropy to our damage model through the introduction of an anisotropic crack driving state function, $\tilde{D}$, that is dependent on the tensile portion of the Cauchy stress, $\boldsymbol{\sigma}^+$, as derived by [Raina and Miehe 2016]:

$$\tilde{D} = \zeta \left\langle \Phi(\boldsymbol{\sigma}^+) - 1 \right\rangle \quad \text{with} \quad \boldsymbol{\sigma}^+ = \sum_{i=1}^{3} \langle \sigma_i \rangle \boldsymbol{n}_i \otimes \boldsymbol{n}_i \tag{7}$$

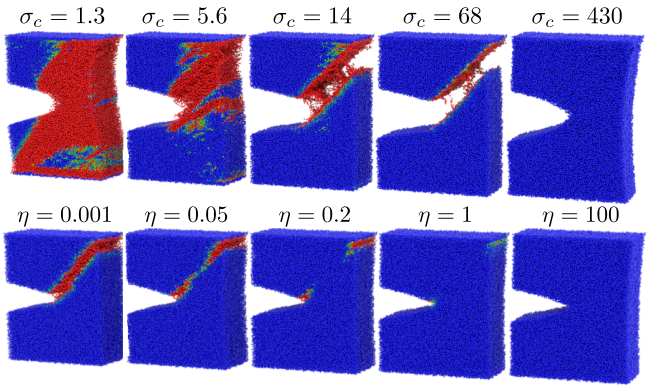

Fig. 10. **Effect of σ_c and η.** Tearing a diagonally fibered block shows that σ_c controls the material's resistance to cracking while η dictates the crack propagation speed. For the top row, $\eta = 0.1$, and for the bottom row, $\sigma_c = 25$.

This ζ controls the slope of the driving force, but we keep it equal to 1 for all explorations to reduce the parameter space. As for $\Phi(\boldsymbol{\sigma}^+)$, we are inspired by the approach of [Raina and Miehe 2016] and derive a highly generalizable expression for adding various forms of anisotropy to our crack driving force:

$$\Phi(\boldsymbol{\sigma}^+) = \frac{1}{\sigma_c^2} (\boldsymbol{A}\boldsymbol{\sigma}^+ : \boldsymbol{\sigma}^+ \boldsymbol{A}). \tag{8}$$

Here, we introduce σ_c, a critical stress threshold that dictates how much stress a material can withstand before fracturing (see Fig. 10 to visualize the fracture effects attainable simply through changing σ_c and η). We also introduce $\boldsymbol{A}$, a second order structural tensor that encodes the material's fiber directions. If we let $\boldsymbol{a_1}$ be the principal fiber direction, and $\boldsymbol{a_2}$ be the secondary fiber direction (in the case of orthotropy) we define $\boldsymbol{A}$ as:

$$\boldsymbol{A} = \boldsymbol{I} + \alpha_1(\boldsymbol{a_1} \otimes \boldsymbol{a_1}) + \alpha_2(\boldsymbol{a_2} \otimes \boldsymbol{a_2}), \tag{9}$$

where $\boldsymbol{I}$ is the identity matrix, α_1 is a variable controlling the strength of the principal fiber direction's influence on fracture, and α_2 the same for the secondary fiber direction. These α parameters weight the influence of each material direction and dictate the nature of the anisotropy. Through this general form we can define structural tensors for isotropic materials ($\alpha_1 = \alpha_2 = 0$), transversely isotropic materials ($\alpha_1 \neq 0, \alpha_2 = 0$), and orthotropic materials ($\alpha_1 \neq 0, \alpha_2 \neq 0$). See Fig. 4 to visualize how these three types of materials respond to dynamic fracture. We do not explore the material effects achievable through tuning these scalars (to reduce parameter space); we instead consider them to have values $\alpha_i \in \{-1, 0\}$ where a value of -1 indicates the fiber has the strongest possible control over the fracture direction and 0 indicates the fiber has no influence whatsoever. Finally, see Fig. 11 for a visualization of the crack driving force, $\tilde{D}$, using a variety of fiber directions and Fig. 12 to see the various material effects possible simply through changing the material fiber direction.

3.3 Elasticity Degradation

We couple our anisotropic damage with anisotropic elasticity through degrading relevant terms in the anisotropic energy density, $\Psi(\boldsymbol{F})$, using a monotonically decreasing function of the damage, $g(d)$; this is a common approach shared by many phase-field methods [Ambati et al. 2016; Borden et al. 2016; Miehe et al. 2010a,b; Wolper et al. 2019]. Specifically, we degrade only the tensile portion of the isotropic elasticity associated with the material's isotropic matrix:

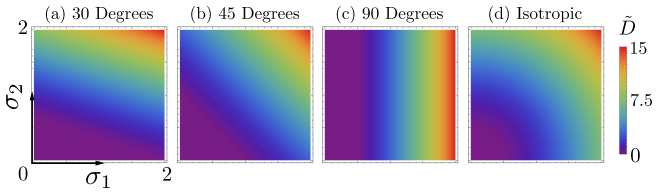

Fig. 11. **Effect of Fiber Direction on $\tilde{D}$.** We plot in Cauchy stress space the crack driving state function, $\tilde{D}$, for four fiber directions to show the directional effect on $\tilde{D}$. This function has directionality for a fibered material (a,b,c) while isotropic materials have the same $\tilde{D}$ in all directions (d).

Ψ^+. We do not degrade the compressive portion of the matrix energy, Ψ^-, nor the fiber energy, Ψ^f. This gives an expression for the degraded energy density, $\hat{\Psi}(\boldsymbol{F})$, as:

$$\hat{\Psi}(\boldsymbol{F}) = g(d)\Psi^+(\boldsymbol{F}) + \Psi^-(\boldsymbol{F}) + \Psi^f(\boldsymbol{F}), \tag{10}$$

with $g(d) = ((1-d)^2(1-r)) + r$ including the residual stress, r, to ensure a small tensile stress even in regions of full damage and prevent degenerate deformation gradients. This quadratic degradation function is used by many CDM approaches to fracture due to its simplicity, its monotonically decreasing nature, and its correct scaling for both a fully damaged ($g(1) = r$) and a fully healthy ($g(0) = 1 + r$) material [Miehe et al. 2015; Wolper et al. 2019]. See §5 for more details on our anisotropic elasticity and refer to Fig. 20 to visualize this concept of elasticity degradation.

4 ANISOMPM SPATIAL DISCRETIZATION

4.1 Traditional MPM

MPM is a hybrid method comprised of meshless quadrature points that carry Lagrangian physical quantities (traditionally, quantities like m, $\boldsymbol{x}$, $\boldsymbol{v}$, and $\boldsymbol{F}$, but, for AnisoMPM, we also have damage d, fiber directions $\{\boldsymbol{a}\}$, and fiber magnitudes $\{\alpha\}$) in conjunction with a background grid that is used to compute spatial derivatives. Here, we present the traditional MPM pipeline (see [Jiang et al. 2016] for details) to both elucidate the basic data flow as well as highlight the augmentations that make up AnisoMPM.

First, we transfer mass and momentum from particles to grid using APIC [Jiang et al. 2015]. Second, we use our anisotropic elasticity and user defined boundary conditions to compute forces and update grid velocity. We then transfer information back from the grid, update particle velocities, and advect particle positions. Finally, we update the deformation gradients and process them with return mapping for plasticity (see Fig. 14). To enable anisotropy, the core augmentation we need is in the grid velocity update, in which we employ elasto-damage coupling to update grid velocity and perform our inextensibility solve if desired (see Fig. 13).

4.2 AnisoMPM Data Flow

Instead of coupling damage with momentum in a prohibitively long monolithic solve we choose to adopt a staggered integration scheme in which damage is updated first, and then, the new damage is used to update grid velocities to resolve momentum. This scheme has recently shown great success for fracture in graphics and mechanics [Amor et al. 2009; Miehe et al. 2015; Wolper et al. 2019] and in practice, we find it typically requires only a single staggered iteration to adequately converge and produce visually striking results. In Fig. 13, we present the entirety of our AnisoMPM data flow, seeking to highlight the core differences from traditional MPM (the damage pipeline, elasto-damage coupling, and inextensibility). The damage pipeline always begins with transferring damage from the particles to the grid but branches into two paths, depending on whether we want to solve damage using explicit or implicit integration. Both of these branches end with our damage updated to d^{n+1}, and we pair this damage with our anisotropic constitutive model (using elasticity degradation) to compute forces on the grid that are then used for updating grid velocity; this can be seen as replacing $\frac{\partial \Psi}{\partial \boldsymbol{F}}(\boldsymbol{F}_p^n)$ with $\frac{\partial \Psi}{\partial \boldsymbol{F}}(\boldsymbol{F}_p^n, d^{n+1})$ in the grid update step of MPM (see §5 for more details on elasto-damage coupling). Finally, inextensibility is incorporated into AnisoMPM as a hard-constrained grid velocity solve, and note that this can be easily turned on or off as it is completely modular within the data flow. Note that anisotropic elasticity does not explicitly appear in the data flow, but is instead encoded in the grid velocity update as our constitutive energy density function, $\Psi(\boldsymbol{F})$. Plasticity is also easily added to this pipeline through return mapping our updated $\boldsymbol{F}_p$, as demonstrated in Fig. 14.

4.3 Damage Evolution

We track our phase-field damage variables, d, on the particles and transfer them to and from the grid similarly to momentum. In this way, we represent continuum cracks by tracking particle damage in world space and evolving it using grid computations (see Fig. 15).

We develop novel MPM-based discretizations of Eqn. (6) using both explicit and implicit time integration, each bringing unique numerical benefits. Implicit damage has the advantage of taking much larger time steps, encoded in our damage model through the crack mobility constant η; thus, implicit damage is capable of producing extremely fast cracks through its ability to use significantly smaller η values, as evidenced in Fig. 16. However, in practice, our explicit

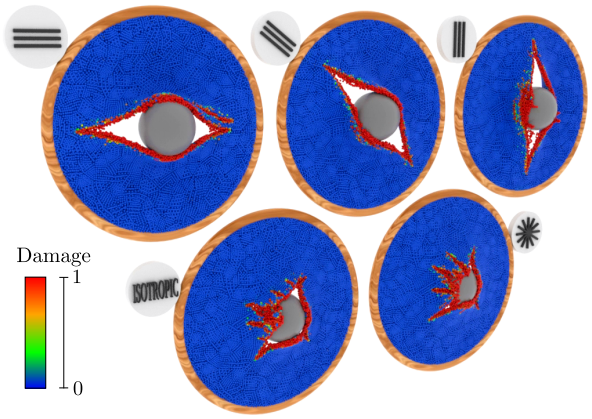

Fig. 12. **Disk Shoot.** A sphere pushes through disks initialized with a variety of fiber directions, illustrating the wide variety of material affects achievable. Note the color denotes the damage variable, $d \in [0, 1]$, with blue being healthy material and red being fully damaged material; the color bar is to give an idea of the range of colors, but the particle colors come from ramping damage values. Note that the bottom right shows radial fibers.

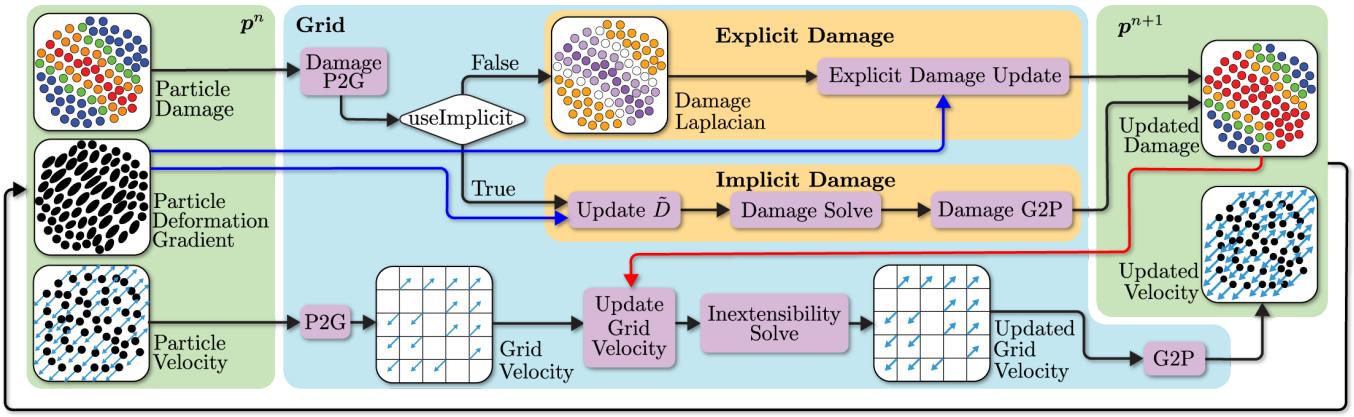

Fig. 13. **AnisoMPM Data Flow.** We illustrate the AnisoMPM data flow including both explicit and implicit damage. Additionally note the blue arrows show that we need to use F_p^n to update damage regardless of method, and the red arrow shows that we must solve for damage before the dynamics because we need the damage to compute forces for our grid velocity update. Finally, note that inextensibility is a post process on grid velocity that can be turned on or off.

damage integration benefits not only from its comparative ease of implementation, but also achieves better computational speeds due to the lack of lengthy system solves (despite smaller time steps), avoids numerical damping, and produces qualitatively similar results. Note that the material fiber directions, $\{\boldsymbol{a}_i\}_p$ are constant per particle during simulation; thus, we use the rotation, $\boldsymbol{R}_p^n$, of $\boldsymbol{F}_p^n = \boldsymbol{R}_p^n \boldsymbol{S}_p^n$ to update the rotation of these fibers, leading to the following updated construction rule for our structural directors:

$$\boldsymbol{A}_p^n = \boldsymbol{I} + \alpha_1(\boldsymbol{R}_p^n \boldsymbol{a}_1 \otimes \boldsymbol{R}_p^n \boldsymbol{a}_1) + \alpha_2(\boldsymbol{R}_p^n \boldsymbol{a}_2 \otimes \boldsymbol{R}_p^n \boldsymbol{a}_2).$$

See our supplemental document [Wolper et al. 2020] for thorough pseudocode for both explicit and implicit damage evolution.

4.3.1 Explicit Integration. We discretize Eqn. (6) with explicit time integration to produce the following local damage evolution rule:

$$d_p^{n+1} = \min\left(1, d_p^n + \frac{\Delta t}{\eta}\langle(1 - d_p^n)\tilde{D}_p^n - (d_p^n - l_0^2 \Delta d_p^n)\rangle\right), \qquad (11)$$

where we take the min with 1 to enforce $d \in [0, 1]$, and where $\tilde{D}_p^n$ is the maximum value in the history of particle p's driving force, $\tilde{D}_p^H$, such that $\tilde{D}_p^n = \max(\tilde{D}_p^H, \zeta\langle\Phi(\boldsymbol{\sigma}_p^{+n}) - 1\rangle)$. Computing the Laplacian, Δd_p^n, requires that we transfer the damage to the grid:

$$\Delta d_p^n = \sum_i d_i^n \Delta N_i^n \quad \text{with} \quad d_i^n = \frac{\sum_p w_{ip}^n d_p^n}{\sum_p w_{ip}^n},$$

and $\Delta N_i^n = N_i''(x)N_i(y)N_i(z) + N_i(x)N_i''(y)N_i(z) + N_i(x)N_i(y)N_i''(z)$ where $N_i(\boldsymbol{x}_p)$ is the interpolation function used for transfer. Note that this computation requires the second derivative, mandating that we use at least cubic $N_i(\boldsymbol{x}_p)$. Additionally, we choose FLIP to transfer damage to avoid the numerical diffusion inherent to PIC, and the need for additional resources dictated by APIC.

4.3.2 Implicit Integration. Now we discretize Eqn. (6) with implicit time integration to produce an implicit damage evolution rule:

$$\left(1 + \frac{\Delta t}{\eta}(\tilde{D}^n + 1)\right) d^{n+1} - \left(\frac{\Delta t}{\eta} l_0^2\right) \Delta d^{n+1} = \frac{\Delta t}{\eta}\tilde{D}^n + d^n. \qquad (12)$$

Note that this requires updating $\tilde{D}$ first to enforce the crack irreversibility. We further discretize Eqn. (12) by writing a weak form of the PDE and then using the MLS shape function [Hu et al. 2018a], $\Theta_i(\boldsymbol{x})$, and its gradient, $\nabla\Theta_i(\boldsymbol{x}_p) = M_p^{-1} w_{ip}^n (\boldsymbol{x}_i - \boldsymbol{x}_p^n)$ to get a positive semi definite linear system for the unknown d_i^{n+1} (see [Wolper et al. 2020]):

$$(\mathcal{A} + \mathcal{B})\boldsymbol{d} = \boldsymbol{c}, \qquad (13)$$

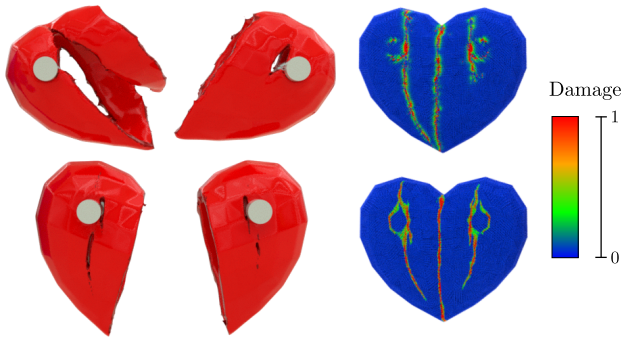

Fig. 14. **Broken Heart.** We break a soft flow-fibered plastic heart with von Mises plasticity (above, $\tau = 4$) both to show the natural coupling between AnisoMPM and plasticity as well as to compare with a purely elastic run (below) to highlight the plastic deformation only possible with the former.

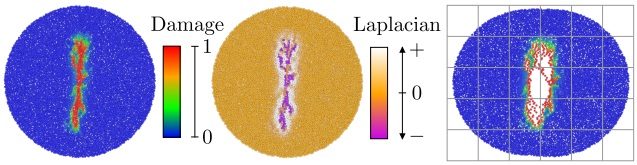

Fig. 15. **Damage Discretization.** We tear a disk to show our damage discretization. (Left) In material space, each particle carries a damage variable, $d \in [0, 1]$. (Middle) We visualize Δd's influence on damage evolution. (Right) In world space the crack propagates as highly damaged particles separate.

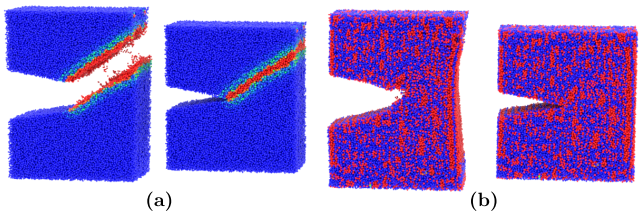

Fig. 16. **Implicit vs. Explicit Damage.** We use a very small mobility constant ($\eta = 1 \times 10^{-9}$) to produce a very fast crack front and compare the results using (a) implicit damage and (b) explicit damage. This illustrates that explicit damage is incapable of resolving extremely fast cracks without making the time step prohibitively small while implicit damage can.

where $\boldsymbol{d}$ is the vector of unknowns, d_i^{n+1}, and with:

$$\mathcal{A} = [\mathcal{A}_{ii}] = \sum_p V_p^n \left(1 + \frac{\Delta t}{\eta}(\tilde{D}_p^n + 1)\right) w_{ip}^n$$

$$\mathcal{B} = \left[\mathcal{B}_{ij}\right] = \sum_p V_p^n \left(\frac{\Delta t}{\eta} l_0^2\right) \left(\nabla\Theta_i(\boldsymbol{x}_p^n)\right)^T \left(\nabla\Theta_j(\boldsymbol{x}_p^n)\right)$$

$$\boldsymbol{c} = [c_i] = \sum_p V_p^n \left(\frac{\Delta t}{\eta}\tilde{D}_p^n + d_i^n\right) w_{ip}^n$$

Here, $\mathcal{A}$ is a diagonal matrix, $\mathcal{B}$ is the MPM discrete Laplace operator, and $\mathbf{c}$ is the vector of right hand terms. We can solve this system using the conjugate gradient method preconditioned with the Jacobi preconditioner due to its heat equation-like form [Gao et al. 2018b; Stomakhin et al. 2014; Wolper et al. 2019]. In practice, this requires under two iterations to reach near-roundoff accuracy.

5 ANISOTROPIC ELASTICITY

5.1 QR-Elasticity

Drawing inspiration from [Jiang et al. 2017], we design our anisotropic hyperelastic constitutive model through QR-decomposition of the deformation gradient $\boldsymbol{F} = \boldsymbol{QR}$, where $\boldsymbol{Q}$ is a rotation and $\boldsymbol{R}$ is upper-triangular such that:

$$\boldsymbol{R} = \begin{pmatrix} r_{11} & r_{12} & r_{13} \\ & r_{22} & r_{23} \\ & & r_{33} \end{pmatrix}.$$

We write our additively-decomposed anisotropic energy as:

$$\Psi(\boldsymbol{R}) = \Psi^{\mu}(\boldsymbol{R}) + \Psi^{\lambda}(\boldsymbol{R}) + \Psi^{f}(\boldsymbol{R})$$

where $\Psi^{\mu}(\boldsymbol{R}) = \frac{\mu}{2}(\sum_{ij} r_{ij}^2 - dim) - \mu(J-1)$ is the *shearing term*, $\Psi^{\lambda}(\boldsymbol{R}) = \frac{\lambda}{2}(J-1)^2$ is the *volumetric term*, and with $J = \det(\boldsymbol{F})$. This design comes from the stable Neo-Hookean energy [Smith et al. 2018]. In the original model, there is also a logarithmic term that helps ensure meta-stability under degeneracy, but we omit this term because, as we will show, our anisotropic design already ensures there is no degenerate local optimum on the energy manifold.

To enable anisotropy (including orthotropy), we add two terms to penalize stretching in the primary fiber direction with stiffness k_x and, optionally, stretching in the secondary fiber direction (orthogonal to the first) with stiffness k_y, i.e. $\Psi^{f}(\boldsymbol{R}) = \frac{k_x}{2}(r_{11}-1)^2 + \frac{k_y}{2}(\sqrt{r_{12}^2 + r_{22}^2} - 1)^2$. This is the *fiber term* (see Fig. 17 to visualize isotropic, transverse isotropic, and orthotropic elasticity); note that this model is similar to that of Teran et al. [2003] but with an additional orthotropic term and added efficiency from our QR approach. In practice, we set stiffness parameters k_x and k_y by multiplying μ with a fiber scale parameter, γ, to make it more intuitive (see Fig. 18 for the influence of E and γ, and Fig. 20 to visualize the γ-scaled energy density). When $r_{11} = 0$, the derivative of our anisotropic term, $-\frac{\partial \Psi^f}{\partial r_{11}} = k_x > 0$, points in the direction of the recovering material's rest shape; naturally, $-\frac{\partial \Psi}{\partial r_{11}}$ does the same, effectively avoiding getting trapped in a degenerate configuration during simulation (see Fig. 19b).

Jiang et al. [2017] proved that given $\Psi = \Psi(\boldsymbol{R})$, the symmetric matrix $\boldsymbol{Q}^T \frac{\partial \Psi}{\partial \boldsymbol{F}} \boldsymbol{R}^T$ shares the same upper triangular part with $\frac{\partial \Psi}{\partial \boldsymbol{F}} \boldsymbol{R}^T$, which is trivially derivable from the expression of $\Psi(\boldsymbol{R})$. Then, we can accordingly compute the first Piola-Kirchhoff stress $\boldsymbol{P} = \frac{\partial \Psi}{\partial \boldsymbol{F}}$. We leave the detailed computation of the stress differential and derivative to the supplemental document [Wolper et al. 2020].

Our anisotropic elasticity energy design has several advantages that lead to better performance than existing models. First, our elasticity model is efficient for computing forces with explicit MPM since no SVD-decomposition is needed. Our tests show that QR-elasticity is over 3.4× faster than a fixed-corotated elastic model. Similarly, we can easily achieve orthotropy in our model. Additionally, note that while we can define the fiber terms using the columns of $\boldsymbol{F}$, we find it is still more efficient to use QR for the isotropic terms; as such, we define all terms using $\boldsymbol{R}$ for unity and clarity.

Furthermore, our anisotropic elasticity is robust to inversions, as both the energy density and the stress are well defined over the whole domain, and our local minimum is attained if and only if $\boldsymbol{F}$ is a rotation (including $\boldsymbol{F} = \boldsymbol{I}$). This enables us to simulate challenging scenes with extreme deformation or inversion (see Fig. 19).

5.2 Elasticity Degradation

We perform our elasto-damage coupling through elasticity degradation. Specifically, we use the degradation function $g(d) \in [0, 1]$ (see §3.3) to *degrade* the tensile contribution of the hyperelasticity, Ψ^+, to allow for material separation under tension while still enforcing material resistance to compression. We additively decompose our

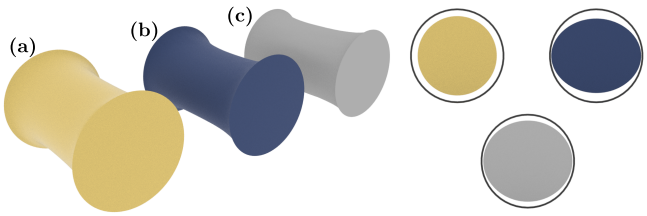

Fig. 17. **Elastic Tube Pull** We stretch a tube with (a) isotropic, (b) transverse isotropic, and (c) orthotropic elasticity. The cross sections at right reveal the material anisotropy: (a) has equal compression, (b) shows less compression along the fiber scaled horizontal direction ($\gamma = 15$), and (c) shows similar behavior to (b) (keeping horizontal $\gamma = 15$), but additionally scales the secondary direction to reduce compression in the vertical direction ($\gamma = 3$).

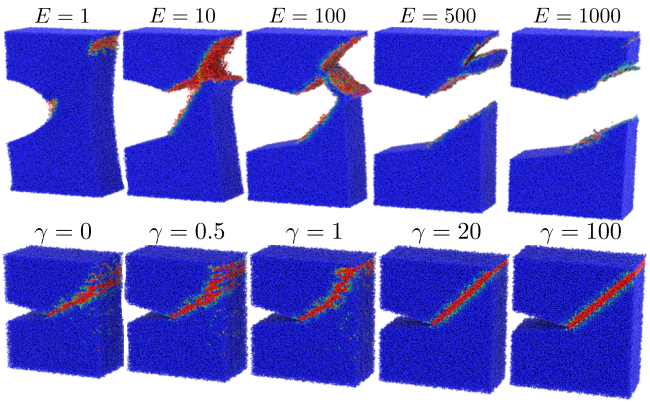

Fig. 18. **Effect of E and γ.** We show in world space that increasing Young's modulus increases material fracture resistance; in material space we illustrate that increasing the fiber scale, γ, gives sharper fracture paths.

QR-elasticity into $\Psi(\boldsymbol{R}) = \Psi^+(\boldsymbol{R}) + \Psi^-(\boldsymbol{R}) + \Psi^f(\boldsymbol{R})$ like so:

$$\Psi^+(\boldsymbol{R}) = \begin{cases} \Psi^\mu(\boldsymbol{R}) + \Psi^\lambda(\boldsymbol{R}) & J \geq 1 \\ \Psi^\mu(\boldsymbol{R}) & J < 1 \end{cases}, \quad \Psi^-(\boldsymbol{R}) = \begin{cases} 0 & J \geq 1 \\ \Psi^\lambda(\boldsymbol{R}) & J < 1 \end{cases}.$$

Notice that we unconditionally include the shearing term in the tensile contribution but include only the volumetric term when $J \geq 1$, indicating an increase in volume. Thus, by Eq. (10), this means we always degrade the shearing term, conditionally degrade the volumetric term, and never degrade the fiber term. Notice that we choose to only degrade the isotropic part of the elasticity, meaning that AnisoMPM predominantly models materials with negligible fiber fracture tendencies (fibers separate but do not tear). However, it is an interesting extension to explore modeling a separate degradation for the fiber terms to allow for fiber breakage under extreme conditions. See Fig. 20 to see how damage affects our QR-energy as it increases.

6 INEXTENSIBILITY

Although our anisotropic elasticity model generally provides visually-plausible results, it may still have difficulty resolving extremely stiff materials (see Fig. 21). Due to the soft constraint approach intrinsic to our constitutive model, we struggle to model high stiffness

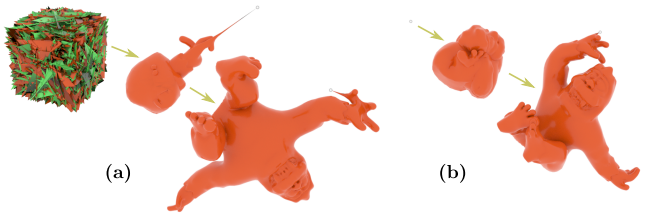

Fig. 19. **Inversions and Extreme Deformations.** We use mesh-based linear FEM to show that our QR-elasticity is robust under extreme circumstances. We show that both (a) a randomly initialized configuration and (b) a one-point initialized configuration can recover the rest shape of the gorilla and model accurate dynamics (assuming the absence of plasticity).

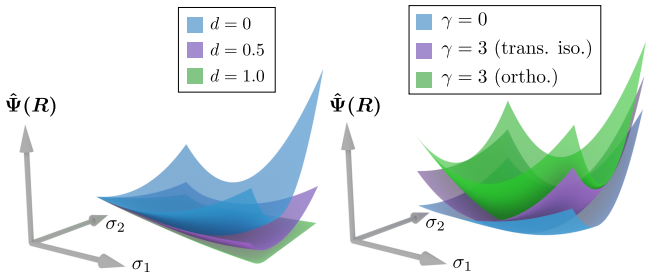

Fig. 20. **Anisotropic Elasticity Visualized.** (Left) We plot our QR-energy density for three damage values in Cauchy stress space, illustrating the degrading energy as damage increases. (Right) We show the energy density for three fiber scales, γ, corresponding to isotropic, transverse isotropic, and orthotropic elasticity. Note the asymmetry of the transverse isotropic energy compared to orthotropic's symmetric scaling.

materials without significantly decreasing Δt for explicit MPM. Similarly, the system may even be too stiff to solve using implicit MPM. Furthermore, even if the system were solvable, it may still suffer from the classic *locking* effect (see Fig. 22). To avoid this difficulty, we present an embedded directed inextensibility solver in which extreme stiffness is modeled with hard constraints. Note throughout this section that we assume the inextensible fibers embedded in the continuum to only transform under rigid kinematics. By using polar decomposition to extract the closest rotation $\boldsymbol{R}$ to the local deformation gradient $\boldsymbol{F}$, we assign the world space fiber direction to be $\boldsymbol{R}\boldsymbol{a}_1$. Also recall that fibers are co-located with material points, whose $\boldsymbol{F}$ is updated with $\nabla \boldsymbol{v}$ as usual. In this way, our inextensibility routine requires no additional fiber modeling or treatment than what AnisoMPM already provides.

6.1 Theory and Equations

We follow [O'Bradaigh and Pipes 1991] to formulate our inextensibility enforcing constraint equation in Eulerian space as follows:

$$(\boldsymbol{a} \otimes \boldsymbol{a}) : \boldsymbol{d} = 0, \tag{14}$$

where $\boldsymbol{d} = \frac{1}{2}\left(\frac{\partial \boldsymbol{v}}{\partial \boldsymbol{x}} + \frac{\partial \boldsymbol{v}}{\partial \boldsymbol{x}}^T\right)$ is the Eulerian rate-of-strain tensor and $\boldsymbol{a} = \boldsymbol{a}(\boldsymbol{x}, t)$ is the current unit fiber direction in Eulerian space. We leave the derivation of this to the supplemental document [Wolper et al. 2020]. Supposing we are at a certain time step, we solve our governing equation with the above constraint to update grid velocities. Our constrained conservation of momentum equation is:

$$\rho(\boldsymbol{x}, t)\frac{D\boldsymbol{v}}{Dt} = \nabla^{\boldsymbol{x}} \cdot \boldsymbol{\sigma}_{\text{full}} + \rho(\boldsymbol{x}, t)\boldsymbol{g}, \tag{15}$$

where $\boldsymbol{\sigma}_{\text{full}} = \boldsymbol{\sigma} + \lambda(\boldsymbol{a} \otimes \boldsymbol{a})$ is the full stress, $\lambda = \lambda(\boldsymbol{x}, t; \boldsymbol{a})$ represents the unknown tension along the fiber direction enforcing the inextensibility constraint, and $\boldsymbol{\sigma}$ is the isotropic stress from the constitutive model. Our goal is to construct a system to solve for $\boldsymbol{v}$ and λ.

6.2 Weak Form

We follow [Jiang et al. 2016] to derive the weak form for our equations. We will use α, β as the dimension indices, i as the traditional MPM grid index, and z as the grid cell index. For convenience, we

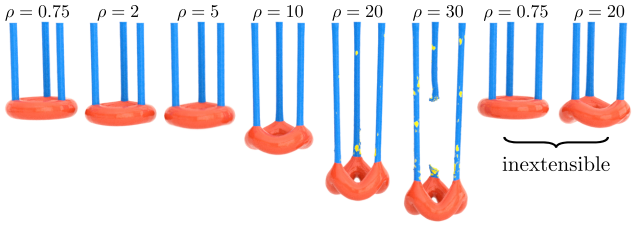

Fig. 21. **Hanging Torus.** For the left six tori we simulate the ropes with anisotropic elasticity, whereas the right two have ropes simulated with inextensibility. Across runs we increase the density of the torus to demonstrate that for a constant time step and fiber scale, anisotropic elasticity numerically fractures for heavier tori, whereas inextensibility remains steadfast.

also use the subscript $i\alpha$ to denote the α dimension of grid i. We define N_n to be the number of MPM grid nodes and N_c to be the number of MPM grid cells.

6.2.1 Momentum equation. By multiplying Eq. (15) by our test function $\boldsymbol{q}(\boldsymbol{x}, t)$, integrating in world space, and applying integration by parts and divergence theorem (ignoring gravity and assuming a zero-traction boundary for simplicity), we have:

$$\int_{\Omega^t} q_\alpha \rho \frac{Dv_\alpha}{Dt} d\boldsymbol{x} = -\int_{\Omega^t} q_{\alpha,\beta}\sigma_{\alpha\beta} d\boldsymbol{x} - \int_{\Omega^t} q_{\alpha,\beta}\lambda a_\alpha a_\beta d\boldsymbol{x}, \quad (16)$$

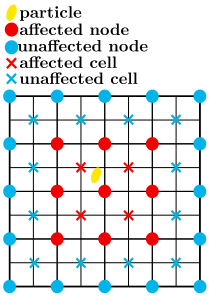

where summation over index α, β is implied. We expand velocity and q at nodes, λ at cell centers using B-Spline (note that we use two sets of basis, N is quadratic at nodes whereas Γ is linear at cell centers) to get: $q_\alpha(\boldsymbol{x}) = q_{i\alpha}N_i(\boldsymbol{x}), v_\alpha(\boldsymbol{x}) = v_{i\alpha}N_i(\boldsymbol{x}), \lambda(\boldsymbol{x}) = \lambda_z\Gamma_z(\boldsymbol{x})$. The figure on the left illustrates the effect of particles on grid nodes and cell centers. Circles represent grid nodes while crosses represent cell centers, and red denotes non-zero weights. We pick $q_{i\alpha} = \delta_{(i,\alpha)=(i^*,\alpha^*)}$ to get one equation for each degree of freedom for each grid node. After simplification, we get the final form of our momentum equation:

$$\frac{m_i}{\Delta t} v_{i\alpha}^{n+1} + B_{(z,i\alpha)}\lambda_z = b_{i\alpha}, \quad (17)$$

where the coefficients are $B_{(z,i\alpha)} = \int_{\Omega^{t^n}} a_\alpha(\boldsymbol{a}\cdot\nabla N_i)\Gamma_z(\boldsymbol{x})d\boldsymbol{x}$, and $b_{i\alpha} = \frac{m_i}{\Delta t}v_{i\alpha}^n - \int_{\Omega^{t^n}} N_{i,\beta}(\boldsymbol{x})\sigma_{\alpha\beta}(\boldsymbol{x}, t^n)d\boldsymbol{x}$. This gives us $dim \times N_n$ equations of $v_{i\alpha}^{n+1}$ and λ_z.

6.2.2 Constraints. We similarly manipulate Eq. (14) by introducing the test function, $h(\boldsymbol{x}, t)$, to get a variational problem:

$$\int_{\Omega^t} h(\boldsymbol{x}, t)(\boldsymbol{a}\otimes\boldsymbol{a}) : \boldsymbol{d} d\boldsymbol{x} = 0. \quad (18)$$

Once again, we interpolate our equation over grid nodes and cells to get: $v_\alpha(\boldsymbol{x}) = v_{i\alpha}N_i(\boldsymbol{x})$ and $h(\boldsymbol{x}) = h_z\Gamma_z(\boldsymbol{x})$. We let $h_z = \delta_{z=z^*}$ (in turn picking an equation for each cell center). Simplifying, we get:

$$\int_{\Omega^t} \Gamma_c(\boldsymbol{x}) a_\alpha a_\beta v_{i\alpha}\frac{\partial N_i(\boldsymbol{x})}{\partial x_\beta} d\boldsymbol{x} = 0. \quad (19)$$

Extracting the $v_{i\alpha}$ term, we derive our linear constraint equations:

$$B_{(z,i\alpha)}v_{i\alpha} = 0, \quad (20)$$

giving us N_c equations of $v_{i\alpha}^{n+1}$ and λ_z.

6.3 Discretization and Implementation

As shown above, the equations are discretized over the MPM grid (both nodes and cells). We further discretize the integration in $b_{i\alpha}$ and $B_{(z,i\alpha)}$ over the particles following standard MPM, resulting in:

$$\int_{\Omega^{t^n}} N_i(\boldsymbol{x})\sigma_{\alpha\beta}(\boldsymbol{x}, t^n)d\boldsymbol{x} \approx \sum_p V_p^n \sigma_{p\alpha\beta}^n N_{i,\beta}(\boldsymbol{x}_p), \quad (21)$$

$$\text{and } B_{(z,i\alpha)} \approx \sum_p V_p^n \Gamma_z(\boldsymbol{x}_p) a_\alpha(\boldsymbol{a}\cdot\nabla N_j(\boldsymbol{x}_p)). \quad (22)$$

Assembling the above equations, we present our linear system as:

$$\begin{pmatrix} \boldsymbol{M} & \boldsymbol{B}^T \\ \boldsymbol{B} & O \end{pmatrix}\begin{pmatrix} \boldsymbol{v} \\ \boldsymbol{\lambda} \end{pmatrix} = \begin{pmatrix} \boldsymbol{b} \\ 0 \end{pmatrix} \quad (23)$$

where $\boldsymbol{M}$ is a $(dim \times N_n) \times (dim \times N_n)$ diagonal matrix where the $(i\alpha, i\alpha)$ element equals $\frac{m_i}{\Delta t}$, $\boldsymbol{b}$ is a $(dim \times N_n) \times 1$ vector with $i\alpha$-th element equal to $b_{i\alpha}$ in Eq. (17), and $\boldsymbol{B}$ is a $N_c \times (dim \times N_n)$ sparse matrix with its $(z, i\alpha)$ element equal to $B_{(z,i\alpha)}$.

This is a sparse and symmetric KKT system and is not positive-definite. In practice, we do not need to directly solve this system. We eliminate $\boldsymbol{v}$ and solve $\boldsymbol{\lambda}$ via $\boldsymbol{B}\boldsymbol{M}^{-1}\boldsymbol{B}^T\boldsymbol{\lambda} = \boldsymbol{B}\boldsymbol{M}^{-1}\boldsymbol{b}$. One can easily verify that this is equivalent to solving the original system. Note that $\boldsymbol{M}$ is a diagonal matrix with positive entries; hence, $\boldsymbol{M}, \boldsymbol{M}^{-1}, \boldsymbol{B}\boldsymbol{M}^{-1}\boldsymbol{B}^T$ are all symmetric semi-positive definite, which we then can solve with the conjugate gradient method and compute $\boldsymbol{v}$ to get the inextensibility-constrained grid velocities. This inextensibility solver can be easily integrated into our AnisoMPM pipeline as a hard-constrained grid velocity solve (see Fig. 13). Inextensibility works in tandem with our anisotropic damage and is able to create sharp fracture along any fiber direction (see Fig. 23).

7 RESULTS

We showcase a wide variety of demos to illustrate the sheer magnitude of dynamic anisotropic fracture effects AnisoMPM can produce.

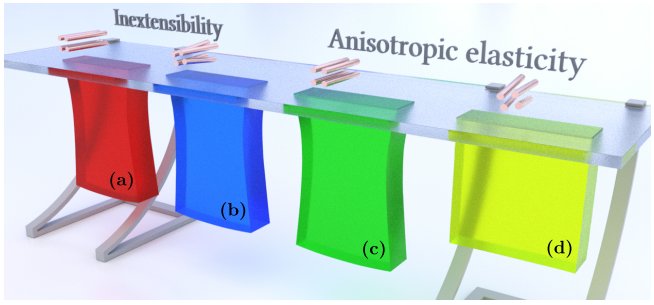

Fig. 22. **Locking.** We hang a jello prism using both inextensible fibers (a,b) and anisotropically elastic fibers (c,d). When the fibers are parallel to one another (a,c) these methods behave the same; however, when the fibers are slightly perturbed (b,d), anisotropic elasticity experiences the common "locking" effect (whereas inextensible fibers are resolved properly).

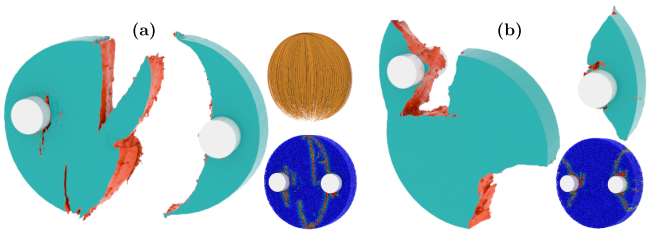

Fig. 23. **Disk Tear.** We tear a disk composed of longitudinal fibers using (a) anisotropic damage and inextensibility (no elasticity), and (b) isotropic damage and elasticity, demonstrating the successful coupling of anisotropic damage and inextensibility.

We list all major demo timings and parameters in Table 1. All simulations were run on an Intel i7-9700K CPU with 8 threads at 3.60 GHz using symplectic Euler time integration for momentum and with $\zeta = 1$, $l_0 = 0.5\Delta x$, and $\alpha = -1$. We will open-source all AnisoMPM code after publication.

We first discuss our illustrative demos, each seeking to highlight a core feature of AnisoMPM. In Fig. 14, we show the seamless incorporation of plasticity into AnisoMPM as well as the plastic behavior only possible through this union. In Fig. 10 and Fig. 18 we exhibit the high degree of artistic control that our AnisoMPM parameters afford artists. In Fig. 4 we show that AnisoMPM is general and robust enough to capture not only isotropic fracture, but also transversely isotropic and orthotropic fracture, as well. We also demonstrate in Fig. 17 that our constitutive model can model isotropic, transversely isotropic, and orthotropic elastic responses. Furthermore, we highlight the inversion safety and robustness of our hyperelasticity in Fig. 19. We also compared our QR-based elasticity with an existing SVD-based model and found ours to be over 3.4× faster at computing the elastic response for 1×10^8 different $\boldsymbol{F}$. Finally, we explore the efficacy of our directed inextensibility solve: in Fig. 22 we show inextensibility to be locking-free; in Fig. 21, we show that inextensibility can resolve extremely stiff materials even under heavy loads that anisotropic elasticity fails under; and, in Fig. 23 and Fig. 9, we show inextensibility to successfully pair with the anisotropic damage. We also note that the KKT system within our inextensibility solve can be easily relaxed by adding a diagonal matrix to the bottom-right block, improving the conditioning of the entire system. Interestingly, we proved in our supplement [Wolper et al. 2020] that the relaxation is theoretically equivalent to applying a soft penalty on the inextensibility constraints, which is similar to modeling inextensibility using QR-elasticity. This reveals that QR-elasticity and inextensibility are both solving the same constrained problem, but utilize soft and hard constraints respectively.

Thus far, we have shown each of AnisoMPM's core components to be successful. However, in Fig. 2 and Fig. 3, we show that the anisotropic damage and anisotropic elasticity should be paired together for best results, as only one method alone fails to produce the robustly-directed fracture that AnisoMPM is clearly capable of. These figures demonstrate that damage alone produces messy, hard to control fractures. Similarly, elasticity alone produces fractures, but these are purely numerical and not controllable in terms of crack propagation speed or physical fracture resistance. In Fig. 2(d) we further highlight that without anisotropic damage, the material experiences extreme deformation before beginning to tear, a highly undesirable property when seeking to artistically harness fracture. In Fig. 9, we showcase a piercing demo with a variety of settings within AnisoMPM, demonstrating the many successful visual possibilities. We further show successful flow-generated fiber guided fracture by skinning a fish in Fig. 6. AnisoMPM even produces convincing real-world bone fractures (seen in Fig. 24) that qualitatively agree with existing medical data [Pierce et al. 2004]. Finally, we present an exciting set of photo-realistically rendered demos produced with AnisoMPM. In Fig. 4, we peel apart the decadent layers intrinsic to dong-po pork belly (rendered using photogrammetry on a real homemade piece). In Fig. 7 we peel apart a cheese stick to reveal the stringy mozzarella fibers. For dessert, we tear a succulent orange slice in Fig. 5 to reveal the jewel-like structures inherent to its radial anisotropy. Finally, in Fig. 1, we tear raw meat along its fiber grain to illustrate the underlying anisotropic muscle fibers.

While AnisoMPM clearly stands as a successful and novel new approach that achieves highly-detailed dynamic anisotropic fracture, it is impossible to ignore direct comparisons with other CDM based MPM approaches such as the recently introduced PFF-MPM [Wolper et al. 2019]. AnisoMPM's key advantage lies not only in its ability to produce isotropic *and* anisotropic fracture (PFF-MPM is strictly isotropic), but also in its introduction of explicit damage evolution, leading to significantly higher efficiency than PFF-MPM (see Fig. 25). While methods do exist to augment PFF with anisotropic damage, it requires the introduction of a fourth-order term that only adds to the complexity of the existing implicit solve (see §2). As such, we believe that AnisoMPM completely eclipses PFF-MPM in terms of generality, efficiency, ease of implementation, and future potential.

Finally, we outline some auxiliary implementation details of AnisoMPM. First, we adopt the novel meshing algorithm of Wang et al. [2019] to produce high fidelity meshes from MPM particles that can be beautifully rendered with no trade offs related to fracture detail and surface smoothness. This allows for highly detailed fracture results with relatively few particles (most sims use 500K or less). However, this meshing did not replace OpenVDB as a key tool for AnisoMPM [Museth et al. 2013]. To ensure the best meshing results, we used TetWild tetrahedralization to ensure good distributions of particles for later meshing [Hu et al. 2018b]. Finally, we adopt

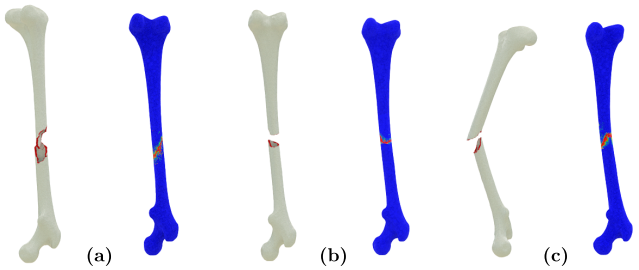

Fig. 24. **Bone Fracture.** We simulate the fracture of a vertically fibered human femur using three different loading scenarios within AnisoMPM: (a) twisting and pulling produces a *spiral fracture*, (b) pulling alone produces a *transverse fracture*, and (c) bending produces an *oblique fracture*. These results qualitatively agree with real-world bone fracture patterns [Pierce et al. 2004]. Note this is one of two demos that uses damage only.

Table 1. **Parameters and Timings.** Seconds per frame is provided as an average with all demos run using symplectic Euler dynamics on an Intel i7-9700K CPU with 8 threads at 3.60 GHz. All parameters are reported in standard CGS units.

Example	s/frame	Δt_{frame}	Δx	Δt_{step}	N	ρ	E	ν	γ	σ_c	η	r
(Fig. 1) Meat	19.30	1/24	6.88×10^{-3}	5.00×10^{-4}	500K	500	5000	0.45	10	3995	0.45	0.1
(Fig. 2) Tube Pull	1.403	1/24	4.38×10^{-2}	1.00×10^{-3}	50K	500	40K	0.45	10	31960	0.45	0.01
(Fig. 3) Tube Compress	83.36	1/24	1.48×10^{-2}	1.00×10^{-4}	400K	2	5000	0.37	10	610.2	0.3	0.01
(Fig. 4) Pork Belly	38.78	1/24	6.92×10^{-3}	2.50×10^{-4}	500K	2	200	0.25	10	17.78	0.1	0.01
(Fig. 5) Orange (int./ext.)	4.890	1/24	7.68×10^{-3}	1.00×10^{-3}	50K/30K	500	10K/50K	0.40	0	2058	0.01	0.001
(Fig. 6) Fish	0.5625	1/48	2.40×10^{-2}	1.00×10^{-3}	50K	1000	100K	0.40	8	35430	0.01	0.1
(Fig. 7) Cheese	48.87	1/24	3.08×10^{-3}	2.00×10^{-4}	500K	500	5000	0.45	10	3537	0.1	0.01
(Fig. 9) Lance (Arma./Ropes)	111.9	1/24	7.81×10^{-3}	1.25×10^{-4}	500K/150K	1/2	100/10	0.30	10/1000	12.67	0.1	0.01
(Fig. 14) Heart	23.88	1/24	9.09×10^{-3}	5.10×10^{-4}	500K	2	100	0.25	3	6.342	0.1	0.01
(Fig. 24) Bone (Bend)	1974	1/48	2.98×10^{-3}	1.00×10^{-6}	200K	800	7×10^8	0.25	0	2.393×10^6	0.1	0.0001

a flow-based fiber generation method in which fluid is simulated through a volume with defined inflows and outflows [Saito et al. 2015]; these flow lines are saved as the material fiber directions (see Figs. 6, 9, 14, and 23 for examples).

8 LIMITATIONS AND FUTURE WORK

As mentioned throughout, AnisoMPM works best when we combine our anisotropic damage and elasticity approaches together; however, there are some rare scenarios we found in which anisotropic damage alone produced more desirable results (bone and orange, see Table. 1). This unpredictability highlights that the many parameters and options available to an artist can make tuning difficult. As such, while this breadth of options does enhance the flexibility of the method and increase the potential for artistic control, there is a steep learning curve that comes with this power. This marks AnisoMPM as an opportune target for the development of a robust interface for artistic control. This would further cement AnisoMPM as a highly general, efficient, and easy to use tool for creating art-directable fracture patterns in any volumetric solid.

Although AnisoMPM produces myriad ductile and dynamic fractures, we did not as thoroughly explore brittle fracture (aside from Fig. 24); however, this likely requires the development of new interpolation functions and treatments and is a prime target for future exploration. Furthermore, AnisoMPM is not designed to produce large-scale debris effects like those seen from plasticity models like NACC [Wolper et al. 2019]; nonetheless, we have already shown AnisoMPM to robustly couple with MPM plasticity (Fig. 14) and, as such, high-debris fracture poses yet another promising target for future work through the development of an anisotropic plasticity scheme. Additionally, while our adopted meshing routine is integral, it still has trouble resolving some intricate details; thus, we propose the exploration of particle resampling techniques like Yue et al. [2015] to treat under-sampled regions and improve meshing.

The components that make up AnisoMPM also have some noteworthy limitations. Explicit damage evolution has restrictions on how small we can make η while maintaining stability, and balancing this CFL condition with the CFL condition related to the momentum solve can be tricky. We seek to resolve this through the additional inclusion of implicit damage; however, implicit damage evolution, in practice, is slower than explicit damage and is also significantly harder to implement. As for elasticity, we have shown that the anisotropic constitutive model struggles to resolve materials of extreme stiffness and is not exempt from numerical fracture; fortunately, our inextensibility method assuages this limitation by treating stiff materials differently. However, despite having some advantages over our constitutive model, our directed inextensibility method is non-trivial to implement and can be slow in practice (with CG the lance demo runs ~1400 s/frame, but we propose exploring efficient solvers like AMGCL) [Demidov 2019].

Despite these shortcomings, AnisoMPM clearly stands as a robust and general approach to animating dynamic fracture of not only isotropic materials, but also the significantly more complex transversely isotropic and orthotropic materials. Furthermore, AnisoMPM offers both the efficient and easy to implement explicit damage and the stable and robust implicit damage, giving flexibility based on the desired fracture behavior and simulation constraints. Finally, we believe AnisoMPM also poses numerous exciting directions for future study, ranging from an intuitive interface for artistic control to the exploration of other types of fracture effects.

ACKNOWLEDGMENTS

We would like to thank Matt Alexander for bringing Fig. 13 to life, Hannah Bollar for narrating the video, C. Jiang's mother-in-law for

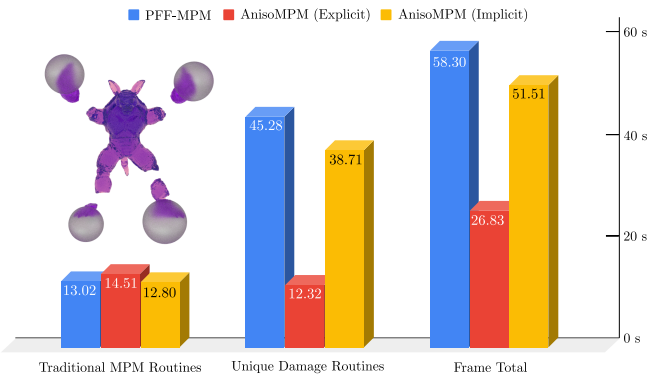

Fig. 25. **Timing Comparison.** We compare timings for an armadillo stretch with three damage methods. We find that implicit AnisoMPM is slightly faster than PFF-MPM [Wolper et al. 2019] while explicit AnisoMPM is significantly faster. Note also that this shows explicit AnisoMPM to add very little computational overhead to the MPM pipeline.

cooking the Dongpo pork model that was scanned and used in Fig. 4, Johan Gaume for useful discussions, and the anonymous reviewers for their valuable comments. This work was supported in part by NSF CAREER (IIS-1943199) and CCF-1813624, DOE ORNL contract 4000171342, the Harlan Stone Fellowship Fund, a gift from Adobe Inc., NVIDIA GPU grants, and Houdini licenses from SideFX.

REFERENCES

M. Ambati, R. Kruse, and L. De Lorenzis. 2016. A phase-field model for ductile fracture at finite strains and its experimental verification. *Comp. Mech.* 57, 1 (2016), 149–167.

L. Ambrosio and V. M. Tortorelli. 1990. Approximation of functional depending on jumps by elliptic functional via t-convergence. *Comm on Pure and App Math* 43, 8 (1990), 999–1036.

H. Amor, J.-J. Marigo, and C. Maurini. 2009. Regularized formulation of the variational brittle fracture with unilateral contact: Numerical experiments. *J. of the Mech. and Phys. of Solids* 57, 8 (2009), 1209–1229.

K. Aoki, N. H. Dong, T. Kaneko, and S. Kuriyama. 2004. Physically Based Simulation of Cracks on Drying 3D Solids. In *Proc. of the Comp. Graph. Int.* 357–364.

I. S. Aranson, V. A. Kalatsky, and V. M. Vinokur. 2000. Continuum field description of crack propagation. *Physical Review Letters* 85, 1 (2000), 118–121.

I. Babuška and M. Suri. 1992. Locking effects in the finite element approximation of elasticity problems. *Numer. Math.* 62, 1 (1992), 439–463.

Z. Bao, J. M. Hong, J. Teran, and R. Fedkiw. 2007. Fracturing Rigid Materials. *IEEE Trans. on Vis. and Comp. Graph.* 13, 2 (2007), 370–378.

G. I. Barenblatt. 1962. The Mathematical Theory of Equilibrium Cracks in Brittle Fracture. Advances in Applied Mechanics, Vol. 7. 55 – 129.

T. Belytschko, D. Organ, and Y. Krongauz. 1995. A coupled finite element-element-free Galerkin method. *Comp. Mech.* 17, 3 (1995), 186–195.

F. Bertails, B. Audoly, M. Cani, B. Querleux, F. Leroy, and J. Lévêque. 2006. Superhelices for Predicting the Dynamics of Natural Hair. *ACM Trans. Graph.* 25, 3 (2006), 1180–1187.

J. Bleyer and R. Alessi. 2018. Phase-field modeling of anisotropic brittle fracture including several damage mechanisms. *Comp Meth in App Mech and Eng* 336 (2018), 213–236.

M. J. Borden, T. J.R. Hughes, C. M. Landis, A. Anvari, and I. J. Lee. 2016. A phase-field formulation for fracture in ductile materials: Finite deformation balance law derivation, plastic degradation, and stress triaxiality effects. *Comp. Meth. in Applied Mech. and Eng.* 312 (2016), 130–166.

M. J. Borden, T. J. R. Hughes, C. M. Landis, and C. V. Verhoosel. 2014. A higher-order phase-field model for brittle fracture: Formulation and analysis within the isogeometric analysis framework. *Comp Meth in App Mech and Eng* 273 (2014), 100 – 118.

S. Bouaziz, S. Martin, T. Liu, L. Kavan, and M. Pauly. 2014. Projective dynamics: fusing constraint projections for fast simulation. *ACM Transactions on Graphics (TOG)* 33, 4 (2014), 154.

B. Bourdin, G. A. Francfort, and J-J. Marigo. 2000. Numerical experiments in revisited brittle fracture. *J. of the Mech. and Phys. of Solids* 48, 4 (2000), 797 – 826.

B. Bourdin, G. A. Francfort, and J.-J. Marigo. 2008. The variational approach to fracture. *Journal of elasticity* 91, 1-3 (2008), 5–148.

J. Brackbill and H. Ruppel. 1986. FLIP: A method for adaptively zoned, Particle-In-Cell calculations of fluid flows in two dimensions. *J Comp Phys* 65 (1986), 314–343.

O. Busaryev, T. K. Dey, and H. Wang. 2013. Adaptive Fracture Simulation of Multi-layered Thin Plates. *ACM Trans. Graph.* 32, 4, Article 52 (2013), 6 pages.

B. Calvo, E. Peña, M.A. Martinez, and M. Doblaré. 2007. An uncoupled directional damage model for fibred biological soft tissues. Formulation and computational aspects. *International journal for numerical methods in engineering* 69, 10 (2007), 2036–2057.

G. Chagnon, M. Rebouah, and D. Favier. 2015. Hyperelastic Energy Densities for Soft Biological Tissues: A Review. *Journal of Elasticity* 120, 2 (01 Aug 2015), 129–160. https://doi.org/10.1007/s10659-014-9508-z

H.Y. Chen, P. Kry, and E. Vouga. 2019. Locking-free Simulation of Isometric Thin Plates. arXiv:cs.GR/1911.05204

J. Chen, H. Bao, T. Wang, M. Desbrun, and J. Huang. 2018. Numerical coarsening using discontinuous shape functions. *ACM Transactions on Graphics (TOG)* 37, 4 (2018), 120.

F. Da, D. Hahn, C. Batty, C. Wojtan, and E. Grinspun. 2016. Surface-only Liquids. *ACM Trans. Graph.* 35, 4, Article 78 (2016), 12 pages.

G. Daviet and F. Bertails-Descoubes. 2016. A Semi-Implicit Material Point Method for the Continuum Simulation of Granular Materials. *ACM Trans. Graph.* 35, 4, Article Article 102 (July 2016), 13 pages.

D. Demidov. 2019. AMGCL: An efficient, flexible, and extensible algebraic multigrid implementation. *Lobachevskii J. of Math.* 40, 5 (01 May 2019), 535–546.

B. Dhas, M. M. Rahaman, K. Akella, D. Roy, and J.N. Reddy. 2018. A phase-field damage model for orthotropic materials and delamination in composites. *J of App Mech* 85, 1 (2018), 011010.

Y. Fang, M. Li, M. Gao, and C. Jiang. 2019. Silly Rubber: An Implicit Material Point Method for Simulating Non-Equilibrated Viscoelastic and Elastoplastic Solids. *ACM Trans. Graph.* 38, 4, Article Article 118 (July 2019), 13 pages.

M. Fassin, R. Eggersmann, S. Wulfinghoff, and S. Reese. 2018. An anisotropic damage and fracture model based on a second order damage tensor.

Y. (R.) Fei, C. Batty, E. Grinspun, and C. Zheng. 2018. A Multi-scale Model for Simulating Liquid-fabric Interactions. *ACM Trans. Graph.* 37, 4 (2018), 51:1–51:16.

G. A. Francfort and J.-J. Marigo. 1998. Revisiting brittle fracture as an energy minimization problem. *J. of the Mech. and Phys. of Solids* 46, 8 (1998), 1319–1342.

M. Gao, A. Pradhana, X. Han, Q. Guo, G. Kot, E. Sifakis, and C. Jiang. 2018a. Animating fluid sediment mixture in particle-laden flows. *ACM Trans. Graph.* 37, 4 (2018), 149.

M. Gao, X. Wang, K. Wu, A. Pradhana, E. Sifakis, C. Yuksel, and C. Jiang. 2018b. GPU Optimization of Material Point Methods. *ACM Trans. Graph.* 37, 6, Article 254 (2018), 12 pages.

D. Garcia-Gonzalez, A. Jérusalem, S. Garzon-Hernandez, R. Zaera, and A. Arias. 2018. A continuum mechanics constitutive framework for transverse isotropic soft tissues. *J of the Mech and Phys of Solids* 112 (2018), 209 – 224.

T. Gerasimov, N. Noii, O. Allix, and L. De Lorenzis. 2018. A non-intrusive global/local approach applied to phase-field modeling of brittle fracture. *Adv Mod and Sim in Eng Sci* 5, 1 (18 May 2018), 14.

R. Goldenthal, D. Harmon, R. Fattal, M. Bercovier, and E. Grinspun. 2007. Efficient Simulation of Inextensible Cloth. *ACM Trans. Graph.* 26, 3, Article 49 (2007).

A. A. Griffith and M. Eng. 1921. VI. The phenomena of rupture and flow in solids. *Phil. Trans. R. Soc. Lond. A* 221, 582-593 (1921), 163–198.

Q. Guo, X. Han, C. Fu, T. Gast, R. Tamstorf, and J. Teran. 2018. A material point method for thin shells with frictional contact. *ACM Trans. Graph.* 37, 4 (2018), 147.

D. Hahn and C. Wojtan. 2015. High-resolution brittle fracture simulation with boundary elements. *ACM Trans. Graph.* 34, 4, Article 151 (2015), 12 pages.

D. Hahn and C. Wojtan. 2016. Fast approximations for boundary element based brittle fracture simulation. *ACM Trans. Graph.* 35, 4, Article 104 (2016), 11 pages.

D. Harmon, E. Vouga, B. Smith, R. Tamstorf, and E. Grinspun. 2009. Asynchronous Contact Mechanics. *ACM Trans. Graph.* 28, 3 (2009), 87:1–87:12.

X. He, H. Wang, and E. Wu. 2018. Projective peridynamics for modeling versatile elastoplastic materials. *IEEE Trans. on Vis. and Comp. Graph.* 24, 9 (2018), 2589–2599.

J. Hegemann, C. Jiang, C. Schroeder, and J. Teran. 2013. A level set method for ductile fracture. In *Proc ACM SIGGRAPH/Eurograp Symp Comp Anim.* 193–201.

K. Hirota, Y. Tanoue, and T. Kaneko. 1998. Generation of crack patterns with a physical model. *The Visual Computer* 14, 3 (1998), 126–137.

K. Hirota, Y. Tanoue, and T. Kaneko. 2000. Simulation of three-dimensional cracks. *The Visual Computer* 16, 7 (2000), 371–378.

M. A. Homel and E. B. Herbold. 2017. Field-gradient partitioning for fracture and frictional contact in the material point method. *Int J for Num Meth in Eng* 109, 7 (2017), 1013–1044.

Y. Hu, Y. Fang, Z. Ge, Z. Qu, Y. Zhu, A. Pradhana, and C. Jiang. 2018a. A moving least squares material point method with displacement discontinuity and two-way rigid body coupling. *ACM Trans. Graph.* 37, 4 (2018), 150.

Y. Hu, Q. Zhou, X. Gao, A. Jacobson, D. Zorin, and D. Panozzo. 2018b. Tetrahedral Meshing in the Wild. *ACM Trans. Graph.* 37, 4, Article Article 60 (July 2018), 14 pages.

G. R. Irwin. 1957. Analysis of Stresses and Strains Near the End of a Crack Traversing a Plate. *J. Appl. Mech.* (1957).

D. Ito, E. Tanaka, and S. Yamamoto. 2010. A novel constitutive model of skeletal muscle taking into account anisotropic damage. *J of the Mech Behavior of Biomed Materials* 3, 1 (2010), 85 – 93.

D. L. James and D. K. Pai. 1999. ArtDefo: Accurate real time deformable objects. In *Proc. of the 26th Ann. Conf. on Comp. Graph. and Inter. Tech.* 65–72.

C. Jiang, T. Gast, and J. Teran. 2017. Anisotropic elastoplasticity for cloth, knit and hair frictional contact. *ACM Trans. Graph.* 36, 4 (2017).

C. Jiang, C. Schroeder, A. Selle, J. Teran, and A. Stomakhin. 2015. The affine particle-in-cell method. *ACM Trans. Graph.* 34, 4 (2015), 51:1–51:10.

C. Jiang, C. Schroeder, J. Teran, A. Stomakhin, and A. Selle. 2016. The material point method for simulating continuum materials. In *SIGGRAPH Course.* 24:1–24:52.

B. Jones, A. Martin, J. A. Levine, T. Shinar, and A. W. Bargteil. 2016. Ductile Fracture for Clustered Shape Matching. *Proc. of the ACM SIGGRAPH symp. on Int. 3D graph. and games* (2016).

L. M. Kachanov. 1999. Rupture Time Under Creep Conditions. *Int. J. of Fracture* 97, 1 (1999), 11–18.

E.G. Kakouris and S.P. Triantafyllou. 2018. Material point method for crack propagation in anisotropic media: a phase field approach. *Archive of Applied Mechanics* 88, 1-2 (2018), 287–316.

E. G. Kakouris and S. P. Triantafyllou. 2017. Phase-field material point method for brittle fracture. *Int. J. for Num. Meth. in Eng.* 112, 12 (2017), 1750–1776.

P. Kaufmann, S. Martin, M. Botsch, and M. Gross. 2008. Flexible simulation of deformable models using discontinuous Galerkin FEM. In *Symp. Comp. Anim.* 105–116.

T. Kim, F. De Goes, and H. Iben. 2019. Anisotropic elasticity for inversion-safety and element rehabilitation. *ACM Transactions on Graphics (TOG)* 38, 4 (2019), 1–15.

G. Klár, T. Gast, A. Pradhana, C. Fu, C. Schroeder, C. Jiang, and J. Teran. 2016. Drucker-prager elastoplasticity for sand animation. *ACM Trans. Graph.* 35, 4 (2016), 103:1–103:12.

C. E. Korenczuk, L. E. Votava, R. Y. Dhume, S. B. Kizilski, G. E. Brown, R. Narain, and V. H. Barocas. 2017. Isotropic Failure Criteria Are Not Appropriate for Anisotropic Fibrous Biological Tissues. *Journal of Biomechanical Engineering* 139, 7 (06 2017).

D. Koschier, J. Bender, and N. Thuerey. 2017. Robust eXtended finite elements for complex cutting of deformables. *ACM Trans. Graph.* 36, 4, Article 55 (2017), 13 pages.

J. A. Levine, A. W. Bargteil, C. Corsi, J. Tessendorf, and R. Geist. 2014. A peridynamic perspective on spring-mass fracture. In *Symp. Comp. Anim.* 47–55.

X. Li, S. Andrews, B. Jones, and A. Bargteil. 2018. Energized rigid body fracture. *Proc. ACM Comput. Graph. Interact. Tech.* 1, 1, Article 9 (2018), 9 pages.

Y. Li and J. Barbič. 2015. Stable anisotropic materials. *IEEE transactions on visualization and computer graphics* 21, 10 (2015), 1129–1137.

Y. Y. Lu, T. Belytschko, and M. Tabbara. 1995. Element-free Galerkin method for wave propagation and dynamic fracture. *Comp. Meth. in Applied Mech. and Eng.* 126, 1 (1995), 131 – 153.

C. Miehe, M. Hofacker, and F. Welschinger. 2010a. A phase field model for rate-independent crack propagation: Robust algorithmic implementation based on operator splits. *Comp. Meth. in Applied Mech. and Eng.* 199, 45-48 (2010), 2765–2778.

C. Miehe, L. M. Schänzel, and H. Ulmer. 2015. Phase field modeling of fracture in multi-physics problems. Part I. Balance of crack surface and failure criteria for brittle crack propagation in thermo-elastic solids. *Comp. Meth. in Applied Mech. and Eng.* 294 (2015), 449 – 485.

C. Miehe, F. Welschinger, and M. Hofacker. 2010b. Thermodynamically consistent phase-field models of fracture: Variational principles and multi-field FE implementations. *Int. J. for Num. Meth. in Eng.* 83, 10 (2010), 1273–1311.

N. Molino, Z. Bao, and R. Fedkiw. 2005. A Virtual Node Algorithm for Changing Mesh Topology During Simulation. In *ACM SIGGRAPH 2005 Courses* (Los Angeles, California). Article 4.

G. Moutsanidis, D. Kamensky, D. Z. Zhang, Y. Bazilevs, and C. C. Long. 2019. Modeling strong discontinuities in the material point method using a single velocity field. *Comp Meth in App Mech and Eng* 345 (2019), 584 – 601.

M. Müller and M. Gross. 2004. Interactive Virtual Materials. In *Proc. of Graphics Interface 2004* (London, Ontario, Canada). 239–246.

M. Müller, T. Kim, and N. Chentanez. 2012. Fast Simulation of Inextensible Hair and Fur. *VRIPHYS* 12 (2012), 39–44.

K. Museth, J Lait, J Johanson, J Budsberg, R Henderson, M Alden, P Cucka, D Hill, and A Pearce. 2013. OpenVDB: An Open-source Data Structure and Toolkit for High-resolution Volumes. In *ACM SIGGRAPH 2013 Courses*. Article 19, 1 pages.

J. A. Nairn. 2003. Material point method calculations with explicit cracks. *Comp. Mod. in Eng. And Sci.* 4 (2003), 649–663.

J. A. Nairn, C. C. Hammerquist, and Y. E. Aimene. 2017. Numerical implementation of anisotropic damage mechanics. *Int J for Numer Meth in Eng* 112, 12 (2017), 1848–1868.

A.N. Natali, P.G. Pavan, E.L. Carniel, M.E. Lucisano, and G. Taglialavoro. 2005. Anisotropic elasto-damage constitutive model for the biomechanical analysis of tendons. *Med Eng & Phys* 27, 3 (2005), 209 – 214.

N. Noii, F. Aldakheel, T. Wick, and P. Wriggers. 2019. An adaptive global-local approach for phase-field modeling of anisotropic brittle fracture. *arXiv preprint arXiv:1905.07519* (2019).

A. Norton, G. Turk, B. Bacon, J. Gerth, and P. Sweeney. 1991. Animation of fracture by physical modeling. *The Visual Computer* 7, 4 (1991), 210–219.

C. M. O'Bradaigh and R. B. Pipes. 1991. Finite element analysis of composite sheet-forming process. *Composites Manufacturing* 2, 3-4 (1991), 161–170.

J. O'Brien, A. Bargteil, and J. Hodgins. 2002. Graphical modeling and animation of ductile fracture. In *Proc ACM SIGGRAPH 2002*. 291–294.

J. F. O'Brien and J. K. Hodgins. 1999. Graphical Modeling and Animation of Brittle Fracture. In *Proc. of the 26th Ann. Conf. on Comp. Graph. and Inter. Tech.* 137–146.

M. Pauly, R. Keiser, B. Adams, P. Dutré, M. Gross, and L. J Guibas. 2005. Meshless animation of fracturing solids. *ACM Trans. Graph.* 24, 3 (2005), 957–964.

T. Pfaff, R. Narain, J. M. de Joya, and J. F. O'Brien. 2014. Adaptive Tearing and Cracking of Thin Sheets. *ACM Trans. Graph.* 33, 4, Article 110 (2014), 9 pages.

M. C. Pierce, G. E. Bertocci, E. Vogeley, and M. S. Moreland. 2004. Evaluating long bone fractures in children: a biomechanical approach with illustrative cases. *Child abuse & neglect* 28, 5 (2004), 505–524.

A. Pradhana, T. Gast, G. Klár, C. Fu, J. Teran, C. Jiang, and K. Museth. 2017. Multi-species simulation of porous sand and water mixtures. *ACM Trans. Graph.* 36, 4 (2017).

A. Raina and C. Miehe. 2016. A phase-field model for fracture in biological tissues. *Biomechanics and modeling in mechanobiology* 15, 3 (2016), 479–496.

D. Ram, T. Gast, C. Jiang, C. Schroeder, A. Stomakhin, J. Teran, and P. Kavehpour. 2015. A material point method for viscoelastic fluids, foams and sponges. In *Symp. Comp. Anim.* 157–163.

S. Saito, Z.-Y. Zhou, and L. Kavan. 2015. Computational Bodybuilding: Anatomically-based Modeling of Human Bodies. *ACM Trans. Graph.* 34, 4 (2015).

C. Schreck and C. Wojtan. 2020. A Practical Method for Animating Anisotropic Elasto-plastic Materials. *Comp Graph Forum - Eurographics 2020* 39, 2 (2020).

P. Shanthraj, B. Svendsen, L. Sharma, F. Roters, and D. Raabe. 2017. Elasto-viscoplastic phase field modelling of anisotropic cleavage fracture. *J of the Mech and Phys of Solids* 99 (2017), 19 – 34.

E. Sifakis, K. G. Der, and R. Fedkiw. 2007. Arbitrary cutting of deformable tetrahedralized objects. In *Symp. Comp. Anim.* 73–80.

S. A. Silling. 2000. Reformulation of elasticity theory for discontinuities and long-range forces. *J. of the Mech. and Phys. of Solids* 48, 1 (2000), 175 – 209.

S. A. Silling and E. Askari. 2005. A meshfree method based on the peridynamic model of solid mechanics. *Computers |& Structures* 83, 17 (2005), 1526 – 1535. Advances in Meshfree Methods.

B. Smith, F. de Goes, and T. Kim. 2018. Stable Neo-Hookean Flesh Simulation. *ACM Trans. Graph.* 37, 2 (2018), 12.

P. Steinmann, C. Miehe, and E. Stein. 1994. On the localization analysis of orthotropic hill type elastoplastic solids. *J of the Mech and Phys of Solids* 42, 12 (1994), 1969 – 1994.

A. Stomakhin, R. Howes, C. Schroeder, and J. Teran. 2012. Energetically consistent invertible elasticity. In *Proc Symp Comp Anim.* 25–32.

A. Stomakhin, C. Schroeder, L. Chai, J. Teran, and A. Selle. 2013. A material point method for snow simulation. *ACM Trans. Graph.* 32, 4 (2013), 102:1–102:10.

A. Stomakhin, C. Schroeder, C. Jiang, L. Chai, J. Teran, and A. Selle. 2014. Augmented MPM for phase-change and varied materials. *ACM Trans. Graph.* 33, 4 (2014), 138:1–138:11.

N. Sukumar, N. Moës, B. Moran, and T. Belytschko. 2000. Extended finite element method for three-dimensional crack modelling. *Int. J. for Num. Meth. in Eng.* 48, 11 (2000), 1549–1570.

N. Sukumar, B. Moran, T. Black, and T. Belytschko. 1997. An element-free Galerkin method for three-dimensional fracture mechanics. *Comp. Mech.* 20, 1 (1997), 170–175.

D. Sulsky, Z. Chen, and H. Schreyer. 1994. A particle method for history-dependent materials. *Comp Meth App Mech Eng* 118, 1 (1994), 179–196.

D. Sulsky, S. Zhou, and H. Schreyer. 1995. Application of a particle-in-cell method to solid mechanics. *Comp Phys Comm* 87, 1 (1995), 236–252.

S. Teichtmeister, D. Kienle, F. Aldakheel, and M.A. Keip. 2017. Phase field modeling of fracture in anisotropic brittle solids. *International Journal of Non-Linear Mechanics* 97 (2017), 1–21.

J. Teran, S. Blemker, V. Ng Thow Hing, and R. Fedkiw. 2003. Finite Volume Methods for the Simulation of Skeletal Muscle. In *Proc of the 2003 ACM SIGGRAPH/Eurographics Symp on Comp Anim* (San Diego, California) *(SCA '03)*. Eurographics Association, 68–74.

D. Terzopoulos and K. Fleischer. 1988. Modeling inelastic deformation: viscoelasticity, plasticity, fracture. *SIGGRAPH Comp Graph* 22, 4 (1988), 269–278.

M. Tournier, M. Nesme, B. Gilles, and F. Faure. 2015. Stable constrained dynamics. *ACM Transactions on Graphics (TOG)* 34, 4 (2015), 132.

B. Wang, Y. Zhao, and J. Barbič. 2017. Botanical materials based on biomechanics. *ACM Transactions on Graphics (TOG)* 36, 4 (2017), 135.

S. Wang, M. Ding, T. F. Gast, L. Zhu, S. Gagniere, C. Jiang, and J. M. Teran. 2019. Simulation and Visualization of Ductile Fracture with the Material Point Method. *Proc. ACM Comput. Graph. Interact. Tech.* 2, 2, Article Article 18 (July 2019), 20 pages.

Y. Wang, C. Jiang, C. Schroeder, and J. Teran. 2014. An adaptive virtual node algorithm with robust mesh cutting. In *Symp. Comp. Anim.* 77–85.

J. Wolper, Y. Chen, M. Li, Y. Fang, Z. Qu, J. Lu, M. Cheng, and C. Jiang. 2020. AnisoMPM: Animating anisotropic damage mechanics: Supplemental document. *ACM Trans. Graph.* 39, 4, Article Article 1 (July 2020), 16 pages.

J. Wolper, Y. Fang, M. Li, J. Lu, M. Gao, and C. Jiang. 2019. CD-MPM: Continuum damage material point methods for dynamic fracture animation. *ACM Trans. Graph.* 38, 4, Article Article 119 (July 2019), 15 pages.

J. Wretborn, R. Armiento, and K. Museth. 2017. Animation of crack propagation by means of an extended multi-body solver for the material point method. *Computers & Graphics* 69 (2017), 131 – 139.

P. Wriggers, J. Schröder, and F. Auricchio. 2016. Finite element formulations for large strain anisotropic material with inextensible fibers. *Advanced Modeling and Simulation in Engineering Sciences* 3, 1 (2016), 25.

Y. Yue, B. Smith, C. Batty, C. Zheng, and E. Grinspun. 2015. Continuum foam: a material point method for shear-dependent flows. *ACM Trans. Graph.* 34, 5 (2015), 160:1–160:20.

Y. Yue, B. Smith, P. Y. Chen, M. Chantharayukhonthorn, K. Kamrin, and E. Grinspun. 2018. Hybrid Grains: Adaptive Coupling of Discrete and Continuum Simulations of Granular Media. *ACM Trans. Graph.* 37, 6, Article 283 (2018), 19 pages.

Y. Zhu and R. Bridson. 2005. Animating sand as a fluid. *ACM Trans. Graph.* 24, 3 (2005), 965–972.

Y. Zhu, R. Bridson, and C. Greif. 2015. Simulating rigid body fracture with surface meshes. *ACM Trans. Graph.* 34, 4, Article 150 (2015), 11 pages.